2019

Frequency analysis of DAV pulsators using TESS data

Cory Daniel Schrandt
Iowa State University

Frequency analysis of DAV pulsators using TESS data

by

Cory Daniel Schrandt

A thesis submitted to the graduate faculty

in partial fulfillment of the requirements for the degree of

MASTER OF SCIENCE

Major: Astrophysics

Program of Study Committee:
Steven Kawaler, Major Professor
Massimo Marengo
Soeren Prell
Dae-Young Lee

The student author, whose presentation of the scholarship herein was approved by the program of study committee, is solely responsible for the content of this thesis. The Graduate College will ensure this thesis is globally accessible and will not permit alterations after a degree is conferred.

Iowa State University

Ames, Iowa

2019

DEDICATION

I would like to dedicate this thesis to my soon-to-be wife, Amanda, without whose support I would not have been able to complete this work. I would also like to thank my friends and family for their loving guidance during the writing of this work.

TABLE OF CONTENTS

Page

LIST OF TABLES

Page

LIST OF FIGURES

Page

ACKNOWLEDGMENTS

I would like to take this opportunity to express my thanks to those who helped me with various aspects of conducting research and the writing of this thesis. First and foremost, Dr. Steven D. Kawaler for his guidance, patience and support throughout this research and the writing of this thesis. I would additionally like to thank him for his passion for teaching and inspiring me to bring that energy into the classroom every day. His insights and words of encouragement have often driven me to push through adversity and achieve my goals. I would also like to thank my committee members for their efforts and contributions to this work: Dr. Massimo Marengo, Dr. Soeren Prell, and Dr. Dae Young Lee.

ABSTRACT

The work presented in this thesis is designed to demonstrate the value and capacities of TESS to contribute to asteroseismology of compact pulsators. I find that TESS data are able to reproduce some of the results obtained by the ground by collaborations like the Whole Earth Telescope (WET) given its ability to observe a star nearly continuously for approximately 27 days. I also address some of the weaknesses of the TESS observations for these purposes, such as the CCD pixel size on the TESS cameras, long integration times, and the bandpass of the telescope's detector. I examined four white dwarf pulsators and found that the MCT 0145-2211 and HE 0532-5605 lack long lifetime modes of pulsation. I place upper limits on the amplitudes of any pulsations in the TESS bandpass. The hottest of the pulsators studied, ZZ Ceti, appeared as expected (after accounting for the TESS bandpass) based on the many ground-based observations of the star. Ultimately the results of this work demonstrate the value of TESS as the next step forward in the field of asteroseismology.

CHAPTER 1. INTRODUCTION

1.1 White Dwarf Pulsators

Low and medium mass stars like the Sun, which make up the majority of the stars in the universe, will eventually evolve into white dwarf stars after puffing off the outer layers of the star following their last time on the giant branch. A white dwarf star is the remnant of the core of the original star (made mostly of carbon and oxygen) surrounded by a thin shell of non-degenerate hydrogen, helium, or, in rare cases, carbon as an atmosphere. The extraordinarily high density (in excess of 10^6 g/cm^3) white dwarf core supports itself against gravity via electron degeneracy pressure which prevents any two electrons from occupying the same quantum state. More massive white dwarfs are smaller because of the increased inwards pressure of gravity reducing the radius until the outwards pressure from electron degeneracy restores equilibrium. While the interior of the white dwarf no longer generates energy via nuclear fusion, the heat built up in the core gradually diffuses outward through the higher opacity outer envelope - thus white dwarfs shine as they cool over time scales of billions of years as first discussed by Mestel (1952), and was later recast by Winget et al. (1987). The effective temperature of white dwarf stars thus drops from over 100000 K to 4000 K or less over time, where the rate of cooling depends on the mass of the star, the efficiency of energy transport through the outer envelope, and how far along it is in the cooling process. Cooling begins rather rapidly but slows down exponentially as the temperature drops lower and lower. In theory, these objects will be able to radiate all of their stored thermal energy away until the core of carbon and oxygen has completely crystallized and the effective temperature aligns with the surrounding space, but this vastly exceeds the lifetime of the universe. Thus the surface temperature of a white dwarf will decrease over time, and as a result, so too will its luminosity.

As this temperature change occurs, there are certain ranges of temperature and surface gravity where the luminosity of the star will be slightly unstable showing pulsations on timescales of minutes

as described in Winget and Kepler (2008). Most white dwarf stars have hydrogen dominated atmospheres and when they reach the instability strip of temperatures for their given surface gravitational acceleration ($\log g$) it is possible to observe periodic oscillations in their brightness due to waves propagating across their surfaces. These non-radial g mode oscillations (where buoyancy is the restoring force) travel through the convection zone of the hydrogen atmosphere. The cause of these waves, discussed by Fontaine and Brassard (2008), is the convective turbulence caused by partial ionization of the thin layer of H changes the opacity of that zone in the stellar atmosphere. This causes build-ups of the temperature in some regions and decreases in others, resulting in periodic brightening and dimming. Some theoretical models attempting to reproduce the observed instability region in the $\log g - T_{\rm eff}$ plane for hydrogen atmosphere white dwarf pulsators (classified as DAV stars) can be found in Van Grootel et al. (2013) reproduced here as Figure 1.1. More acronyms used throughout this paper can be found in Appendix C. White dwarfs with hydrogen dominated atmospheres will pulsate as their temperatures pass between approximately 10 750 K and 13 000 K, though the strip for any given surface gravity is much thinner than that, usually 1000 K or less across. By measuring the oscillations in these stars brightness over extended intervals, we can identify the characteristic frequencies of the oscillations to better explain the physics determining the evolution of these stars.

1.2 Space-Based Asteroseismology

The past decade has ushered in a new era of asteroseismology with the introduction of high precision photometry from various space telescopes, most notably, Kepler and the Transiting Exoplanet Survey Satellite (TESS). These instruments can measure the flux of their target stars down to the parts per million threshold due to the precision and stability of the photometric equipment and the calibration of the data pipeline. This work is important because it can help constrain the mass, radius, inclination, and ages of target stars. Tighter constraints on the physical properties of host stars allows for more accurate measurement of the properties of potential exoplanet candidates that orbit around them.

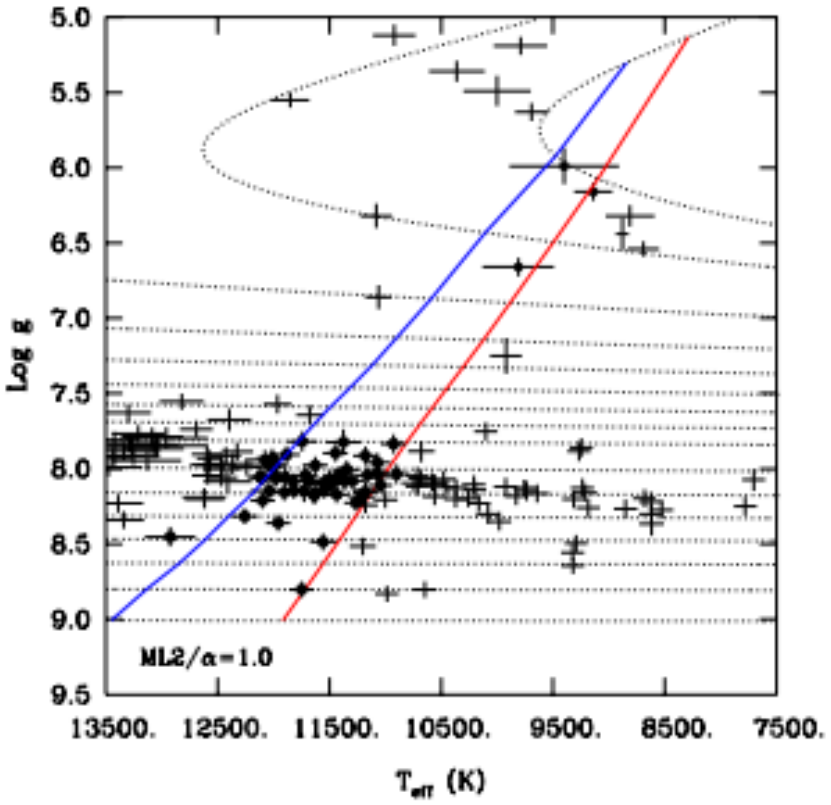

Figure 1.1 A graph of the the theoretical instability strip predicted for DAV stars created by Van Grootel et al. (2013). The crosses indicate nonvariable stars, whereas the filled circles indicate DAVs. The dotted lines show the modelled evolutionary tracks of white dwarfs of different masses. The blue and red curves predict the hot and cool edges of the instability strip respectively for a given surface gravity. Low surface gravity predicts a lower temperature for both the blue and red edges of the strip.

1.2.1 General signal expectations

While the telescopes aboard these spacecraft are significantly smaller than their ground-based counterparts, they do have some major advantages. Though the terrestrial telescopes may have large apertures capable of collecting more flux and in some cases better resolution, they are always susceptible to the weather conditions on Earth. More importantly, an astronomer can hope to get about eight hours of continuous observation from Earth in the best of conditions. Space-based telescopes can remain pointed at their target on a nearly-continuous basis (a very high duty cycle), eliminating the 24 hour cyclical gaps that plague ground-based observations. In addition, the long observation period greatly improves the frequency resolution of the Fourier transforms used to convert the measurements of flux over time into the frequencies of oscillation for the DAV. The basic idea is that the variations in the photometry can be modeled as a summation of sinusoids oscillating at different frequencies and amplitudes. Knowing these frequencies and amplitudes allows for tight constraints to be placed on models of the stars, which in turn constrains the physical properties of the star.

1.2.2 Kepler/K2 successes

The Kepler spacecraft launched in March 2009 and was responsible for the successful detection of thousands of exoplanets via the transit method. Even after the reaction wheels began to fail in 2013, engineers were still able to find a way to keep the pointing of the telescope stable enough to extend Kepler's usefulness via the K2 mission. During the original Kepler mission, the telescope was focused on a 100 square degree field of the sky centered on the constellation Cygnus. Once the K2 mission began, the telescope had to gradually slew to different regions of the sky to remain stable for each campaign because it used solar radiation to stabilize its pointing to compensate for its failed reaction wheels. While K2 was less stable than the initial Kepler mission, it was still successful in detecting hundreds of exoplanets until it was decommissioned in November 2018.

Kepler had two different cadences at which it could collect data on its targets. The short cadence data integrated flux over 58.8 seconds and the long cadence data collected over 29.4 minutes. While

the long cadence data would be sufficient for some science goals, short cadence data was necessary for asteroseismology on DAVs since they usually oscillate with periods of a few minutes, and aliases of signals would be created for periods shorter than the long-cadence sampling time. These would correspond to frequencies higher than roughly 285μHz (more on this later). As discussed in Gilliland et al. (2010), between the long observations capable with this system, the multiple types of cadences available for different types of science, the large field of view of the cameras, and the excellent photometry effective for a wide array of brightness in stars, Kepler (and the following K2 mission) were instrumental to advances in asteroseismology.

1.2.3 TESS: The next step

TESS, launched in 2018, will also be searching for photometric variations in its target stars, but there are a few key differences of note compared to the Kepler mission. TESS will examine nearly the entirety of the sky with an exception for a thin region near the ecliptic plane so that it may avoid the Sun and other bright sources in our solar system. This corresponds to an area of the sky 300 to 400 times larger than the original Kepler field. Some objects located near the ecliptic poles will be observed for nearly one year continuously. The four cameras allow for four regions of the sky to be monitored at once. They are stacked in terms of ecliptic latitude, allowing the ecliptic poles to be continuously covered, while avoiding the ecliptic plane as seen in Figure 1.2 provided by Ricker et al. (2014). TESS is also focused on examining targets that are on average 30 to 100 times brighter than the Kepler targets given the much smaller collecting area per camera, meaning many of the objects are closer than those found in the Kepler field. While that may initially seem limiting, it does allow for easier follow-up observations from ground-based observatories for both asteroseismological and exoplanet candidate targets. Figure 1.3 provides context between the TESS bandpass and common filters for other telescopes. For a sense of scale of the differing brightness of targets, a difference of 2.5 magnitudes means that a target is a factor of 10 dimmer than the reference source as seen in Equation 1.1.

$$M_{star} - M_{ref} = -2.5 * log_{10}(B_{star}/B_{ref}) \tag{1.1}$$

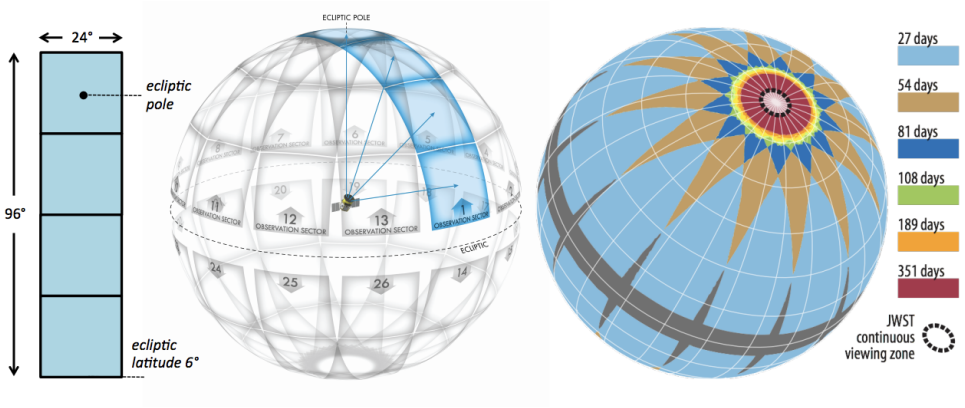

Figure 1.2 The observation window for TESS for each segment of the sky (figure from Ricker et al. (2014)). Note that it spends the largest amount of time observing the ecliptic poles and has some gaps near the ecliptic plane.

The spatial resolution of TESS as described in Campante et al. (2016) is roughly 21.1 arcseconds per pixel. At effectively 1048 x 1048 usable pixels on each of the four cameras, the entire system can view 24°x96°. It orbits Earth twice per 27.4 day sector and conducts its downlink of data while at perigee for roughly 16 hours. This results in a reasonably small gap in the data compared to the overall run length. TESS's bandpass covers a redder part of the electromagnetic spectrum than Kepler as seen in Figure 1.4 partially because in the hunt for exoplanets, it is easier to find Earth-like candidates around the dimmer red dwarf stars cooler than our Sun.

1.3 Comparison with ground-based observations: the Whole Earth Telescope

Ground-based efforts to obtain nearly-continuous photometry of pulsating stars require multiple-site observations. The Whole Earth Telescope (WET) operates as described in Nather et al. (1990), with telescopes distributed at longitudes around the globe all coordinated to observe the same set of targets to minimize the amount of downtime in the duty cycle due to weather and daylight hours. The data coverage needs to be as complete as possible; periodic gaps produce spurious periodicities, the pattern of which is known as the 'window function.' Observing from multiple

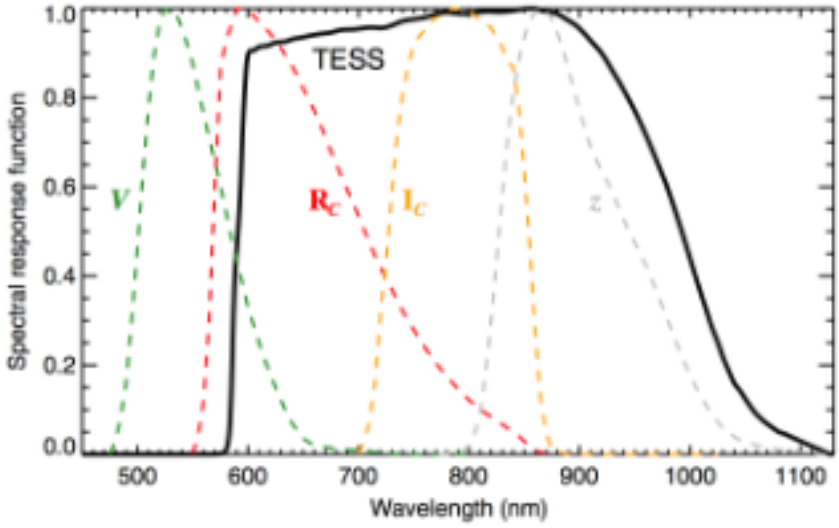

Figure 1.3 A visualization of the types of planets that TESS is expected to be able to find around host stars of given magnitude (figure from Ricker et al. (2014)). It also explains why it is easier for observers to follow up with ground-based observations.

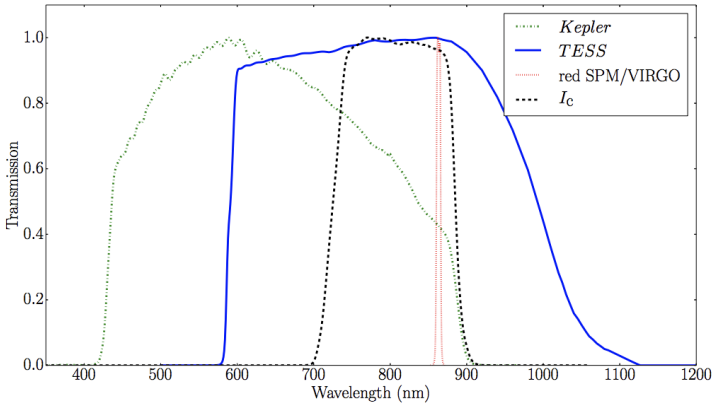

Figure 1.4 An illustration of the difference in the part of the EM spectrum that TESS detectors are sensitive to compared to Kepler and why that type of detector is beneficial to their goal (figure from Campante et al. (2016)).

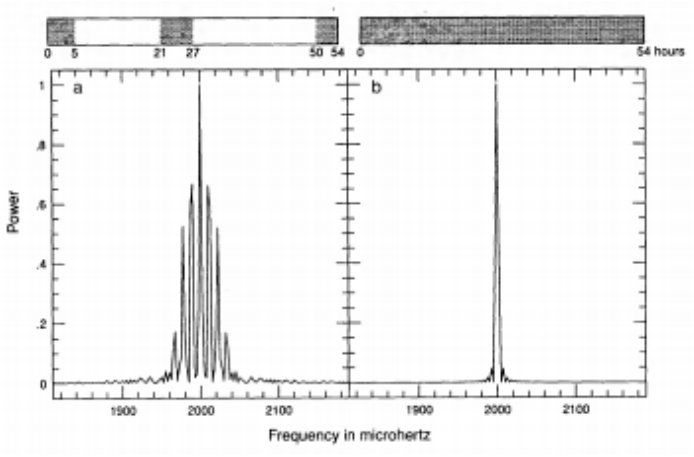

Figure 1.5 A figure from Nather et al. (1990) to show how gaps in the noise-free photometric data produce multiple spikes in the Fourier transform as seen in the left panel. Meanwhile, a continuously observed source oscillating at a single frequency produces the single spike at said frequency.

sites helps minimize this pattern and, in so doing, the window function of the observations is greatly improved as seen in Figure 1.5.

Beyond this, the advent of the WET allowed for larger telescopes to collect enough photons from their targets to allow the oscillations to stand out against the background stochastic and scintillation noise. Without the improved signal-to-noise ratio (SNR) from larger telescopes and those telescopes then coordinating together to resolve possible beat frequencies, asteroseismology on white dwarfs would have been nearly impossible.

1.4 Advantages and Disadvantages

While the efforts of the Whole Earth Telescope were excellent for the tools of the time, the introduction of the space-based telescopes offered great advantages over the earlier work. Even so, there are some issues that ground-based observations can handle better than the space-bound counterparts.

1.4.1 Aliasing from finite sampling - the Nyquist frequency

One issue that has to be addressed is that of aliasing. An aliased signal occurs because the observed signal is limited by the sampling time of the instrument. While the short cadence data from Kepler samples roughly every 60 seconds and TESS samples every 120 seconds, the telescopes in the WET would often sample at 10 or 5 second intervals, meaning that they could distinguish between the reality of a low or high frequency signal more clearly than Kepler or TESS. The frequency over which a low frequency signal and its high frequency alias is reflected is called the Nyquist frequency and is given by Equation 1.2 where Δt is the sampling time per integration.

$$f_{Nyq} = 1/(2\Delta t) \tag{1.2}$$

An example of how this can be problematic is demonstrated in Figure 1.6. Without external knowledge, it is nearly impossible to eliminate this aliasing effect to determine which of these signals is real. While the Nyquist frequency for the short cadence data is out near approximately 8500 μHz which is reasonably far away from most expected frequencies of oscillation for DAVs, TESS's 120 seconds integration times place the Nyquist at 4166.7 μHz instead. This can lead to some complications that are discussed later in Chapter 4.

1.4.2 Faintness

The space telescopes also suffer from only being able to detect targets that fall within certain magnitudes for their given bandpass. Kepler could obtain useful data from sources as faint as 18th or 19th magnitude. TESS is limited to brighter targets because of its smaller aperture, with useful data on white dwarfs that under the best conditions can reach 16th magnitude (in its redder bandpass). Kepler and TESS are limited by the size of their objective mirror and lens respectively. As a result, they end up unable to adapt for follow-up observations of targets of interest that appear too dim for their specifications. Earth based measurements do have the advantage of larger telescopes and the ability to exchange and/or add instruments to follow-up on these targets.

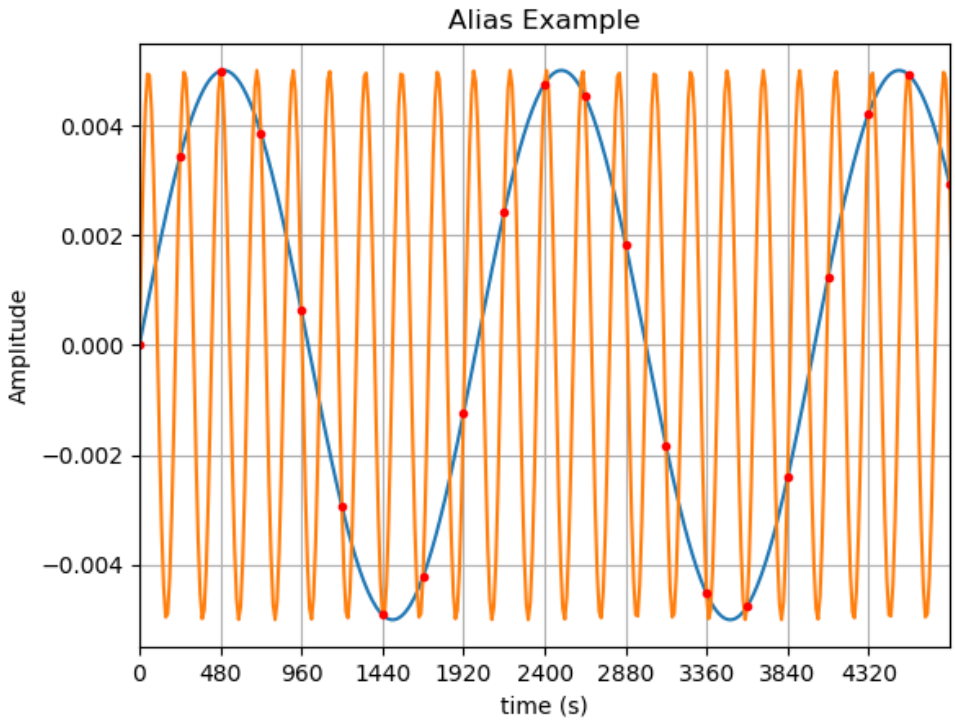

Figure 1.6 A simple illustration demonstrating how a signal that is not sampled frequently enough can be confused for a lower frequency signal. In the diagram, the signal would be sampled every 120 s and the amplitude would be squared to produce a power spectrum. As a result, only the amplitude at every 120 s interval is of interest, labeled with red dots. Because they match up identically at every observation, it is very difficult to separate out the frequency at which the source is oscillating.

1.4.3 Background Contamination

Given that white dwarfs are generally faint targets, the space-based observations are subject to background contamination of other sources. TESS is particularly limited by this crowding issue due to its relatively large pixel size. At roughly 21 arcseconds on a side and the telescope designed to observe cooler objects, it is difficult to not find other sources contaminating the results as the fainter limits of the instrument are approached.

1.4.4 Time Resolution

One of the best advantages granted by the TESS and Kepler missions has been the extremely long observation spans. As mentioned when describing the driving motivation behind establishing the WET, continuous observations over many days allow for the resolution of specific frequencies of oscillation without concern for the daily aliasing caused by gaps in the light curve. The formal frequency resolution of the Fourier transform of the light curve for a regularly sampled light curve is given in Equation 1.3 where Δf is the frequency resolution and ΔT is the run length.

$$\Delta f = 1/\Delta T \tag{1.3}$$

For comparison, an observation over an ideal night of 6 hours of observing the same target continuously with no clouds would allow for a frequency resolution of roughly 46.3 μHz, which may allow for the detection of a high amplitude signal if the observer is lucky. However, if we instead use a typical TESS sector as an example instead with a run length of 27.4 days (with a small gap in the middle), the frequency resolution is close to 0.42 μHz, which easily resolves most peaks.

1.5 Comparing the old ground data to new TESS results

Chapter 2 will explain generally how the data for some previously measured DAVs were collected, reduced, and analyzed. In Chapter 3, the specifics of the analysis of the TESS data for the stars BPM 30551, HE 0532-5605, and MCT 0145-2211 will be compared against their historical ground-based data. The work of Chapter 4 is to reexamine Ross 548, more commonly known by

the name ZZ Ceti for which the class of DAV pulsators was named. This target has been the subject of extensive ground-based study and has some unique characteristics for a TESS target that are treated with some additional careful techniques. A list of all four stars and some of their major properties, including their TESS magnitude and primary archival periods of oscillation, can be found in Table 1.1. Finally, Chapter 5 will recap the ultimate findings of this work as well as encapsulate the benefits of the newly collected TESS data with particular notes of phenomena to be cautious of when reducing its data. It will also provide some insight on the future capabilities of the mission.

Table 1.1 DAVs in this study; periods and amplitudes from Mukadam et al. (2006)

Star	**TIC ID**	**TESS mag**	**Periods (s) \ Amp (mma)**
BPM 30551	102048288	15.81	840.2 \ 11 744.7 \ 10 682.7 \ 13 606.8 \ 15
HE 0532 -5605	382303117	14.94	688.8 \ 8.3 586.4 \ 7.9
MCT 0145 -2211	164772507	15.74	823.7 \ 17 727.9 \ 19 462.2 \ 25
Ross 548 (ZZ Ceti)	029854433	14.18	274.8 \ 3.8 274.3 \ 4.8 213.3 \ 7.4 212.8 \ 4.7

CHAPTER 2. TOOLS AND METHODS FOR DATA REDUCTION

2.1 Target list

The targets were initially compiled by the TESS Astroseismic Science Consortium (TASC) to include all white dwarfs that were bright enough to observe, including known and likely pulsators, along with expected signals from prior research. From this list, my goal was to identify a small group of white dwarfs that were known to pulsate based on prior ground-based studies, and then determine if the same signals could be identified in the TESS data. After checking against the following criteria, I decided to focus on four stars: BPM 30551, HE 0532-5605, MCT 0145-2211, and Ross 548 (more commonly known as ZZ Ceti).

2.1.1 Constraints on sky

When choosing these stars limitations were in place based on the brightness of previously identified DAVs in the first few sectors of the TESS mission. It was also necessary to ensure that they were not contaminated by other sources in the aperture (usually 11x11 pixels). The large pixel size of the CCDs on TESS meant that the light from other bright sources could be within one or two pixels of many targets. The targets of interest in this paper always had at least three pixels of separation (approximately one arcminute) between the central (peak flux) pixel of the target and the peak flux pixel of other sources on the postage stamp provided by the TESS target pixel file (more on this later).

2.1.2 Archive access

The data has been compiled on the Mikulski Archive for Space Telescopes (MAST) for public access. The light curves (including a pre-processed pipeline version) of the simple aperture pho-

tometry were also mirrored on the TASC website. These files are reasonably easy to access and the methods for reducing that data are described in the following section.

2.2 Data reduction pipeline

The data reduction process involves obtaining fluxes, at each time point, for each aperture (11x11 pixels) and selecting the pixel or pixels containing the target star. Next, the process attempts to remove systemic artifacts, bad time points (from cosmic ray strikes and other effects). The end product is a time series of normalized flux values. The code used to perform this data reduction is called `Lightkurve`, and is maintained by the Lightkurve Collaboration; Cardoso (2018).

2.2.1 Standard process

Generally speaking, the process of generating the corrected light curves begins with downloading the target pixel file (TPF) of interest from the MAST. A TPF is an 11x11 postage stamp of pixels from the one of four CCDs per camera that the target landed on. This is basically a small subset of the 1048x1048 array of pixels on each of the CCDs. This TPF is inspected to determine the amount of crowding and other potential bright sources near the target, as seen in Figures 2.1 and 2.2.

After collecting this initial TPF, the next step is to plot the pixels that will be used as the data for the source. The choice provided by the pipeline is often sufficient, but there may be ways to optimize the results. To optimize results, the mask should be made as large as possible to collect all of the signal coming from the target, while keeping the mask from becoming so large that it includes data from sources that are not the target. This maximizes the signal to noise ratio while avoiding introducing non-relevant signals to the data. An example of a pipeline mask is provided in Figure 2.3.

In the cases where the mask is customized to the target star, it is often an iterative process where the first attempted mask may not produce ideal results because crowding may introduce other non-real sources especially due to the large pixel size. For stars as faint as the white dwarfs

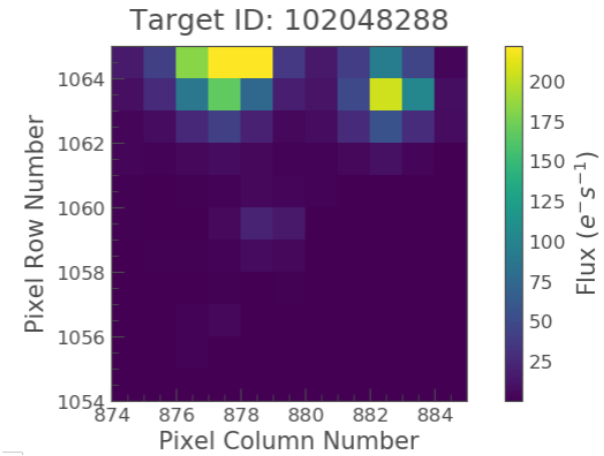

Figure 2.1 A sample target pixel file from BPM 30551 that shows the sampling of an 11x11 pixel grid on the CCD around the target. Each pixel corresponds to approximately 21 arcseconds per side.

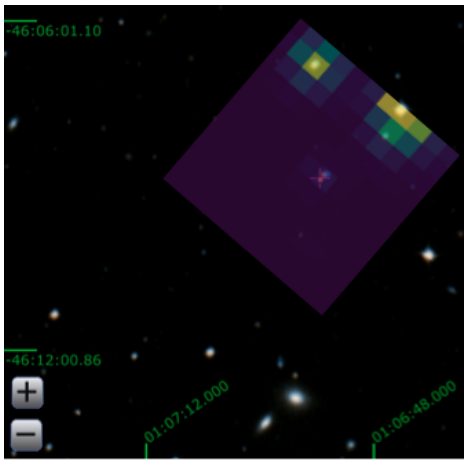

Figure 2.2 The sky surrounding BPM 30551 as provided by the MAST portal. Superimposed on top of that image is a TPF of the star to illustrate the size of TESS's pixels and how significant the contribution of contamination can be.

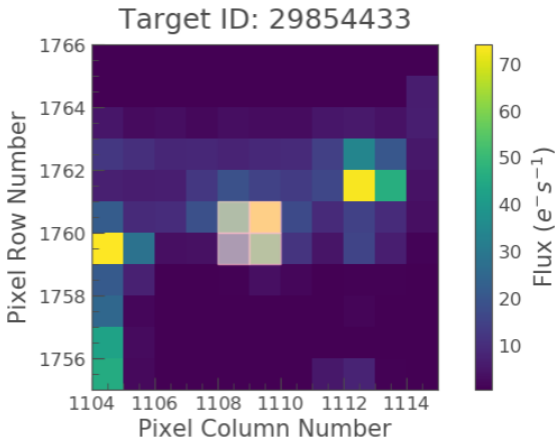

Figure 2.3 An example of the pipeline mask (shaded in translucent white) near the center of the frame. Only the data from those four pixels will be applied to generate the light curve.

in this thesis, a single pixel is usually sufficient unless the frame shows light in more than 1 pixel because of placement of the target near a pixel boundary.

After the mask is chosen for the TPF, the light curve can be generated by simply integrating the flux within the mask as a function of time. The light curve that is initially produced generally may have spurious long-term trends or there are a few outlier data points. Figure 2.4 shows an unreduced light curve. Once the raw light curve is available, there are tools in the `Lightkurve` package which will remove any undefined or spurious data points, flatten the light curve by removing the linear trends in the data set, and perform sigma-clipping that removes any outliers in the data set above a chosen threshold (typically 5σ).

Flattening is generally required due to slight motions of the spacecraft moving some additional flux onto or off of the pixels over the timescale of days. The sigma-clipping is included to make sure any extreme outliers to the data set do not introduce additional low frequency noise to the frequency analysis. After performing these steps, the light curve should look somewhat similar to Figure 2.5. In many cases (including in Figure 2.5), additional steps may be needed to further refine results, as will be discussed in the following sections.

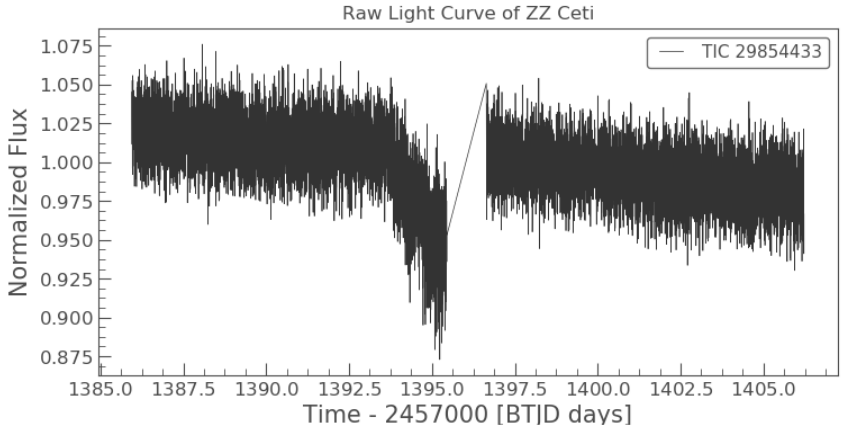

Figure 2.4 An example of the normalized light curve that comes from the TPF. Note the slight downwards slope over time, the gap in the middle of the run caused by the downlink of data, and the region preceding that gap where there is significant deviation from the otherwise linear trend. All of these features should be addressed when considering results.

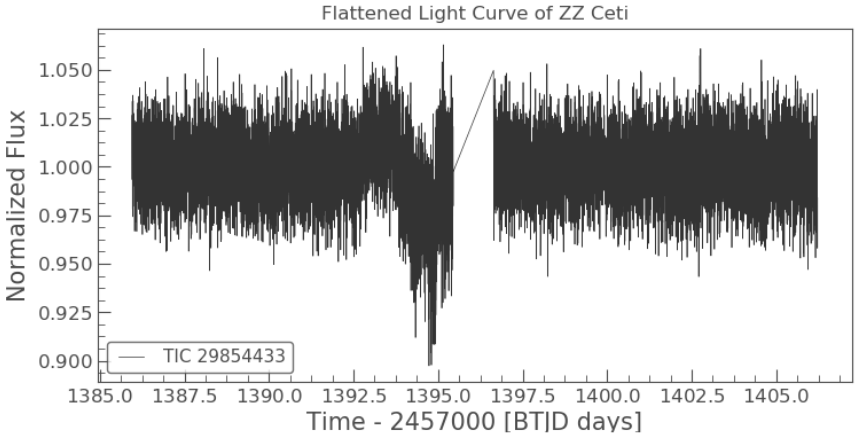

Figure 2.5 Demonstrates how the flatten function of `LightKurve` removes linear trends in the data set. Note that the flattening is not perfect due to the data between roughly 1393 days and 1396 days. Instead, one would trim that data out after confirming that the data in that time frame may have been affected by confounding variables. After that trimming has occurred, then one would apply the flattening and sigma-clipping.

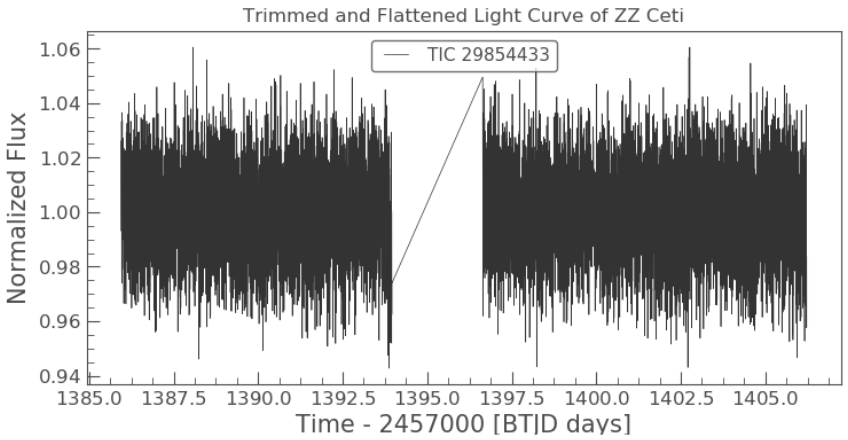

Figure 2.6 Trimmed light curve after removing points flagged in the DRN that has then been flattened and had outlying data points removed. The pulsation signal is not visible in the time series, but emerges from periodogram analysis. This represents data from an "ideal" sector.

2.2.2 Trimming data points

If the data release notes (DRNs) for the sector produced by Fausnaugh et al. (2019) identify sections of the data that are unreliable, it is important to remove those sections from the light curve before performing the flattening and sigma-clipping. If the flattening and sigma-clipping are done first, the shape of the detrending and the level for the outliers would be flawed. Figure 2.6 demonstrates what this final product should look like.

2.2.3 Stitching together multiple sectors of data

If the target of interest is observed in multiple sectors of data, it is possible to extend the run length of the data (and thus improve frequency resolution as seen in Equation 1.3). The comparison of multiple sectors of data on the same target can help determine if the observed signals in the Fourier transforms are long-lived effects, or if they seem to be transient. Before combining each sector together using the append function in `Lightkurve`, each individual sector is subjected to the earlier steps of trimming, clipping out the outlier data points, and finally removing any linear trends for the sector. The final step is to re-normalize the data in each light curve. We are then

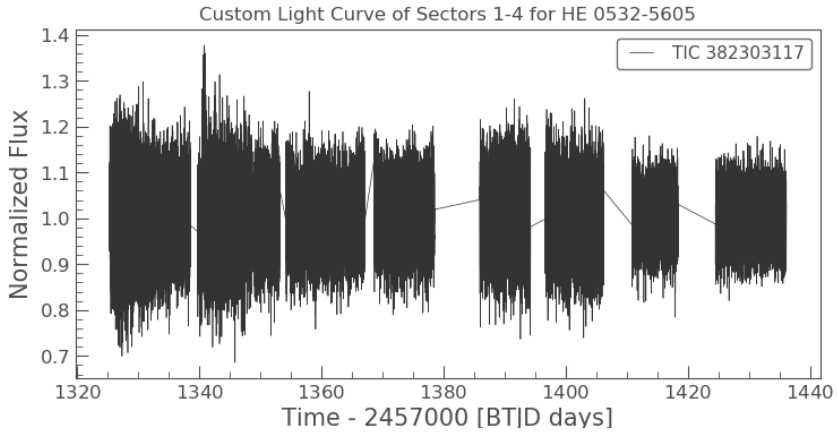

Figure 2.7 The first four sectors of data on HE 0532-5605 all concatenated together after being trimmed, clipped, flattened, and normalized.

able to stitch together the individual sectors to transform the result. An example is provided in Figure 2.7, which features the first four sectors on HE 0532-5605, a star located near the southern ecliptic pole. This allows it to be observed in the first 13 of the 26 total sectors, equating to nearly a year of nearly-continuous coverage.

2.3 Frequency analysis

The spectral components of the time series are determined by Fourier analysis, which yields the amplitude (or power spectrum) of any variability as a function of frequency. An "identified frequency" for the purposes of this thesis is any frequency that rises above four times the mean amplitude (or similarly 16 times the mean power spectrum) which is indicated by a horizontal red dashed line in the periodograms and does not appear to be either an artifact of low frequency noise or an alias of some primary signal. There are numerous features in the Fourier transform that need to be interpreted to ensure that frequencies are correctly identified because they are the final products of interest for asteroseismological models. To ensure that any variability is intrinsic to the target, data from other objects within the target frame can be reduced and analyzed to see if they also show variability at a given frequency. The idea behind this is to perform a quick

inspection using all of the previously described steps to determine whether or not there seem to be any systematically recurring issues on that particular sector of data or on that region of the CCD that did not seem to make its way into the DRN. A set of examples of this may be found in the appendix.

2.3.1 Lomb-Scargle periodogram

The default method provided by the `Lightkurve` for computing Fourier transforms is the Lomb-Scargle periodogram as described in Scargle (1982). This is a helpful method for performing the analysis because it is capable of adapting to uneven spacing in the time series data which will be a feature of all data sets of a given sector simply due to the downlink gap near the middle of the run. There are also all of the data points that would be removed in the trimming from the DRNs and sigma-clipping of outliers that would also contribute to the uneven spacing. The Lomb-Scargle periodogram is far less computationally demanding than the discrete Fourier transform which can take exponentially longer amounts of time as the data sets get longer. For further benefits of the Lomb-Scargle method, see VanderPlas (2017). The resulting periodogram after transforming the light curve generally looks something like Figure 2.8. There is often some low frequency noise which is difficult to remove without careful data reduction of the light curve and noise at all frequencies which arises from the finite signal - the fainter the target, the higher the noise at a given frequency. The data obeys Poisson statistics because the average amount of incoming photons should be relatively constant from background sources and the number of incoming photons at any given time is independent of the number of photons already collected in the same interval. Because the noise follows Poisson statistics, the noise due to any single integration of the incident flux should depend on the square root of the number of counted photons (flux).

2.3.2 Window function for low duty cycle

The window function of a periodogram arises from the fact that the signal being described is a continuous function that is being sampled at finite intervals over a finite amount of time. As

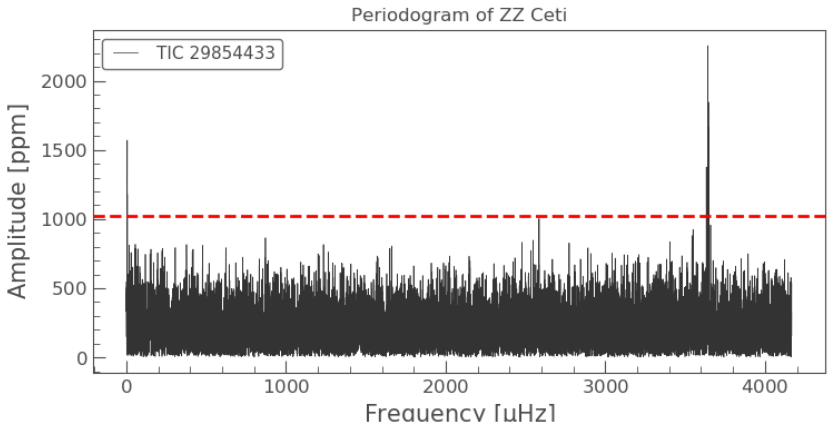

Figure 2.8 A Lomb-Scargle periodogram generated by a reduced light curve.

described in Chapter 3 of VanderPlas (2017), this effectively amounts to a Dirac comb function with peaks that match up with the flux measured at each sampling time convoluted over the rectangular viewing window. Performing a Fourier transform on a Dirac comb function simply produces another Dirac comb of spacing equal to the inverse of the spacing in source function. Examining frequencies beyond the inverse of the spacing of the individual data points (twice the Nyquist frequency as described in Equation 1.2) simply results in repeated aliases of earlier signals and offers no new information. At half of that frequency, aliasing effects are present, as will be discussed in Section 2.3.5. A Fourier transform of the rectangular viewing window results in a *sinc* function with a width inversely proportional to the length of the observing window. Convolution of these two functions results in a *sinc* function centered at each of the frequencies of oscillation. Because the Lomb-Scargle periodogram produces a power spectrum the *sinc* function simply looks like a series of peaks of decreasing amplitude. The results of this can be seen in Figure 2.9, where the side lobes are roughly 0.8 μHz away from the main peak due to the total run length of the data being approximately 20.3 days

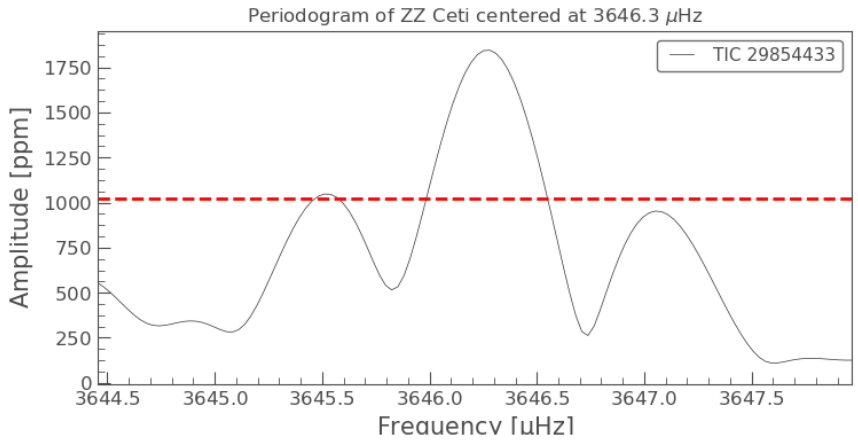

Figure 2.9 One of the signals found in ZZ Ceti at 3646.3 μHz normalized to the amplitude of the signal. The lobes on either side of the main peak show the window function's effect on the data.

2.3.3 Least squares frequency analysis

To obtain precise estimates of frequencies, amplitudes, and phases of periodicities identified via the periodogram, a least-squares fit is valuable. This models individual periodicities as sine (or cosine) curves with fixed frequency, amplitude, and phase. This is similar to the Lomb-Scargle periodogram, but allows for the opportunity to separate out the effects of closely-spaced frequencies on the data set. When frequencies are closely spaced, particularly when their window functions (described in 2.3.2) overlap, it is difficult to determine how much power is present at the frequency at which one is observing, and how much comes from the window function of another nearby frequency. Modeling an individual frequency and being able to subtract out its effects in the time domain enables accurate measurement of the power spectral density of nearby peaks. The amplitudes associated with this analysis will also be included for the stars discussed in this paper to demonstrate the differences between the Lomb-Scargle periodograms produced by `Lightkurve` and this technique.

2.3.4 Examining low frequency signals

As mentioned in Subsection 2.3.1, often there will be some low frequency noise that is nearly impossible to model. However, the low frequency signal could be intrinsic to the target star. For a sense of scale, Table 2.1 provides a list of periods and the frequencies that they correspond to. An example of a possible detected frequency in ZZ Ceti is shown in Figure 2.10. Identifying low frequency signals like this is difficult for instrument configurations like the WET, because the feature would need to be detected over multiple observing sessions. Now with instruments like Kepler and TESS, the long observation time has made detecting low frequencies possible. Being able to detect these low frequency signals is important because it could provide direct measurement of a star's rotation rate.

Table 2.1 Long period oscillations and their corresponding frequencies

Period (hours)	**Frequency (μHz)**
6	46.30
12	23.15
24	11.57
48	5.79
72	3.86

2.3.5 Nyquist frequency

The Nyquist frequency is the frequency beyond which the data are sampled too sparsely to unambiguously distinguish higher frequency oscillations from low frequency modes. During the remainder of this thesis as the results are discussed, there are two relevant features of the Nyquist. First, that the power produced by a frequency is attenuated by the square of the *sinc* function found in Equation 2.1 where Δt is the integration time which for TESS is 120 seconds.

$$\eta(f) = sinc(\pi f \Delta t) = \frac{sin(\pi f \Delta t)}{\pi f \Delta t} \tag{2.1}$$

This means that signals in the super-Nyquist regime are more suppressed than those in the sub-Nyquist. The second important factor is that the power spectral density of the Lomb-Scargle

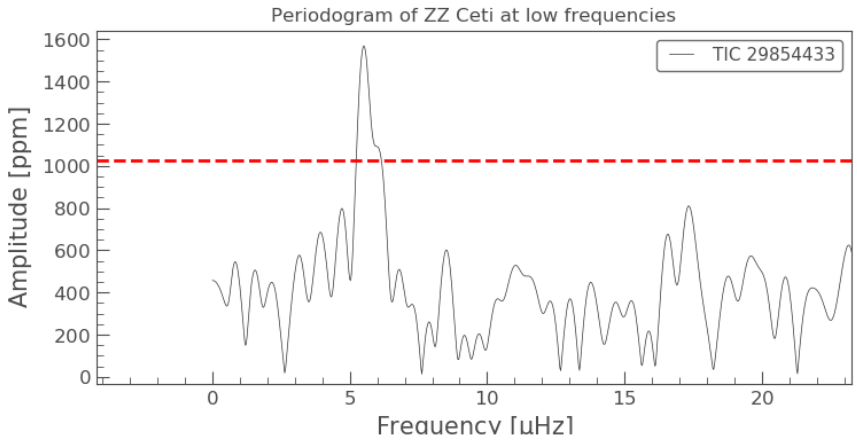

Figure 2.10 One of the signals found in ZZ Ceti at roughly 5.5 μHz normalized to the amplitude of the signal in ppm. The frequency resolution begins to play a big role in the identification of these low frequencies.

periodogram in the `Lightkurve` implementation effectively gets split among its aliases at a given signal. For instance, using Equation 1.2, we know that the Nyquist frequency should be at 4166.7 μHz. This means that a signal 500 μHz away from the Nyquist would appear at both 3666.7 μHz and 4666.7 μHz. If the periodogram extends beyond the Nyquist, some of the power from the 3666.7 μHz peak would be taken into the 4666.7 μHz peak. While this does preserve the relative amplitudes of the surrounding frequencies, it will interfere with the calibration of the absolute power or amplitude associated with each peak. Therefore, most of the remainder of this work will only show the frequencies in the sub-Nyquist regime to accurately represent the power of each peak.

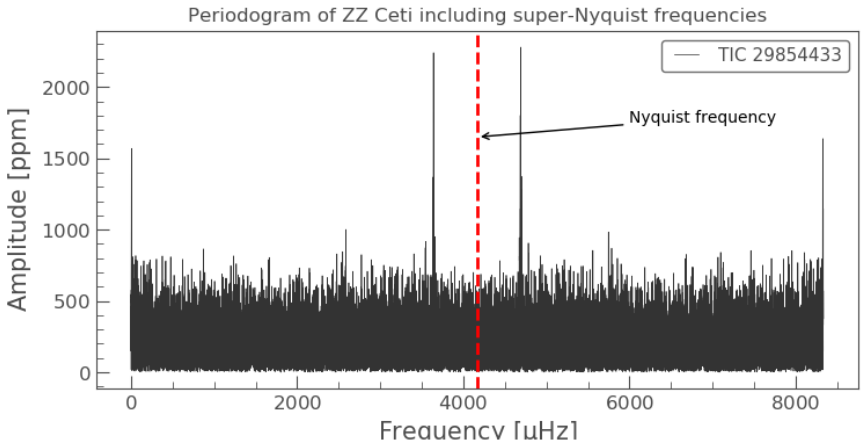

Figure 2.11 The periodogram of ZZ Ceti calculated out to twice the Nyquist frequency. Note the reflection of the signal around 4166.7 μHz indicated by the dashed red line. The small deviation in amplitude on either side comes from how well the real (or its alias) signal lines up with the sampled frequencies used in the periodogram. Also note that the amplitude is significantly lower than that found in Figure 2.9 due to the power being split between the signal and its alias.

CHAPTER 3. PREVIOUSLY ESTABLISHED GROUND-BASED RESULTS AND FINDINGS FROM TESS FOR DAVS NEAR THE COOL EDGE OF THE INSTABILITY STRIP

This chapter explains how earlier ground-based measurements of pulsation frequencies for DAVs were determined and then provides a table of those frequencies. I then compare what the results of the TESS data analysis provides and why that may differ.

3.1 BPM 30551

The white dwarf BPM 30551 was determined to be a pulsator in December 1976 by Hesser et al. (1976). This made it one of the first ten ZZ Ceti stars discovered. It is the dimmest of the target stars in this study, and as such is more susceptible to sources of error.

3.1.1 Ground-based studies

The periods of oscillation were determined to be 606.8, 682.7, 744.7, 840.2 seconds (1648, 1464.8, 1342.8, 1190.2 μHz respectively) in Hesser et al. (1976) where the authors combined 24 subsets of data collected over multiple months. In many of those subsets, the strong signals near 608 and 748 s appeared. The frequencies of the largest peaks and their relative amplitudes for each of the data sets found in Hesser et al. (1976) illustrate the authors' conclusion that BPM 30551 is a complex pulsator with statistically non-stationary processes driving the variations in frequencies.

3.1.2 TESS results in comparison

BPM 30551 (TIC 102048288) was in the Sector 2 field of TESS, which had some of the cleanest data of the first four sectors. The biggest external influence in the data for this star was the presence of two nearby other stars within the same aperture that were many times brighter than

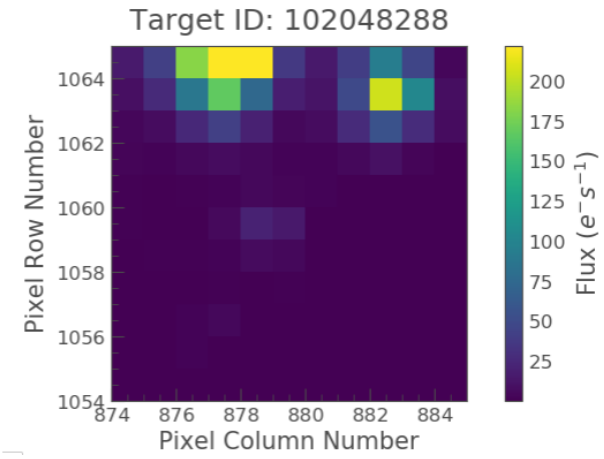

Figure 3.1 The target pixel file for BPM 30551. It is the faint source at the center of the frame. There are two other sources in frame that are many times brighter, but there is enough separation between the two in the sky that it should not dramatically impact the background noise levels or normalization of the data.

the target as seen in Figure 3.1. Using the pipeline mask, which was tightly constrained to just the few pixels receiving flux from the target as seen in 3.2, the influence of these bright neighbors was minimized. BPM 30551 was observed over 25.4 days over a 27.5 day run meaning the duty cycle was over 92.4%. That especially high duty cycle indicates that the window function of the periodogram should be more constrained than the other target stars in this paper which had lower duty cycles (as will be shown later).

As can be seen in the light curve of BPM 30551 in Figure 3.3 after flattening and sigma-clipping, there was no need to trim any of the data points from the set because of the high quality of the data from Sector 2. A great indicator of this quality is the relatively low noise at low frequency seen in Figure 3.4. In 3.5 the window function shows its impact on the signal produced at 1203.4 μHz, causing side lobes to appear approximately 0.7 μHz away from the central peak. Figure 3.6 shows the periodogram after using Equation 3.1 to correct for the attenuation because of averaging over a significant fraction of a pulsation cycle at frequencies near the Nyquist frequency.

$$P(f) = P^*(f) * \eta(f)^2 = P^*(f)\frac{\sin^2(\pi f \Delta t)}{(\pi f \Delta t)^2} \tag{3.1}$$

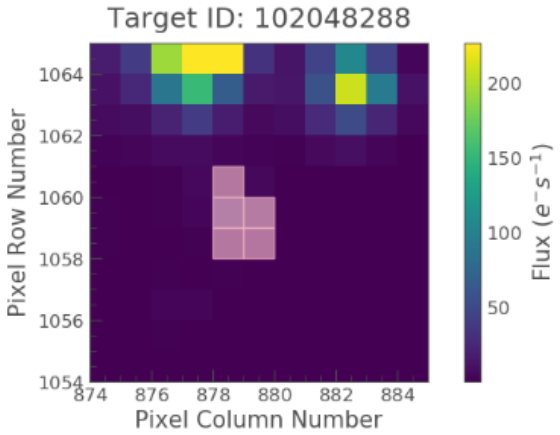

Figure 3.2 The mask used on the target pixel file for BPM 30551.

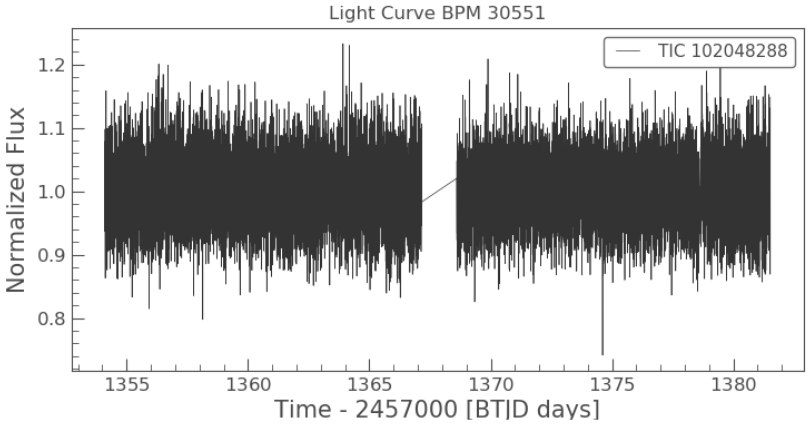

Figure 3.3 The light curve of BPM 30551.

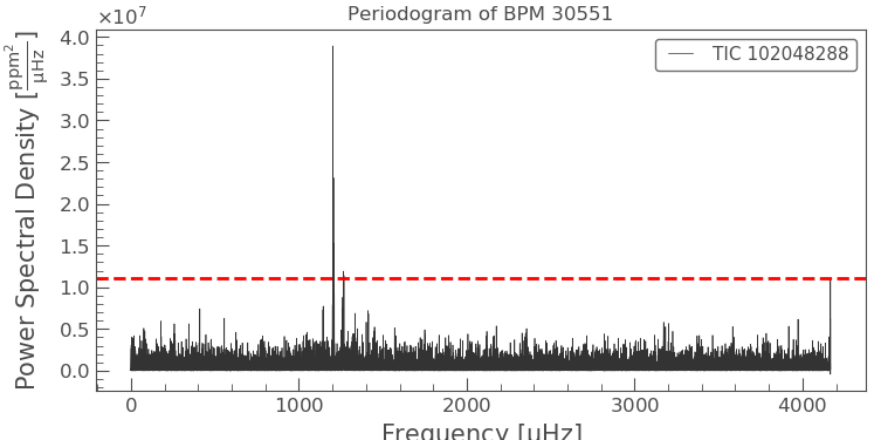

Figure 3.4 The periodogram of BPM 30551. This star has particularly low noise at the low frequencies.

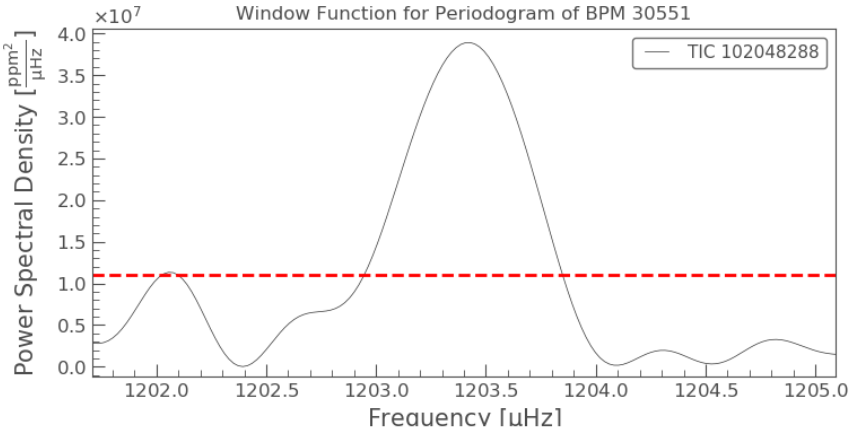

Figure 3.5 The periodogram of BPM 30551 zoomed in on the primary peak at 1203.4 μHz. The side lobes from the window function of this data set are especially reduced in amplitude and separation resulting from the relatively high duty cycle for this sector.

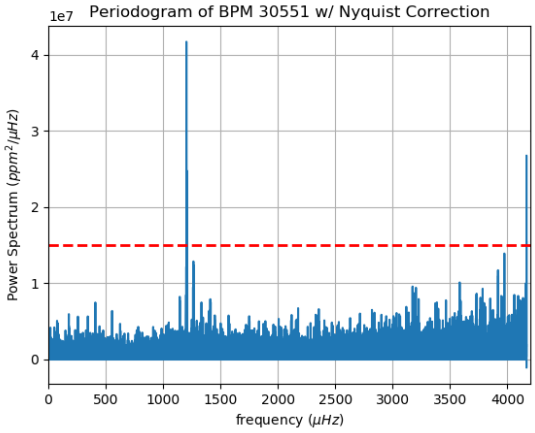

Figure 3.6 The periodogram of BPM 30551 after correcting for the attenuation that occurs due to the Nyquist frequency.

The list of identified frequencies from the TESS data and their power spectral densities are provided in Table 3.1. The power spectral densities are then converted into amplitudes (mma) using Equation 3.2 from Basu and Chaplin (2017) where N is the number of data points in the set. The table also notes the amplitudes as calculated using the least squares analysis and then accounts for attenuation.

$$A(mma) = \sqrt{\frac{2P(\frac{ppm^2}{\mu Hz})}{N\Delta t}} \tag{3.2}$$

Table 3.1 Frequencies of oscillation in BPM 30551.

f (μHz)	**Alias** (μHz)	**PSD** ($ppm^2/\mu Hz * 10^6$)	**Amp** (mma)	**LS Amp** (mma)	**Temp Corr** (mma)
1201.0*	7132.3	8.43	2.77	3.092	4.45
1202.1	7131.2	12.11	3.32	n/a**	5.34
1203.4***	7129.9	41.68	6.16	6.371/6.823	9.90
1206.6	7126.7	24.76	4.75	4.566	7.63
1208.3	7125.0	16.30	3.85	3.657	6.19
1264.5*	7068.8	12.84	3.42	3.108	5.50
1268.3*	7065.0	12.31	3.35	n/a**	5.38

*Below the signal threshold, but detected in least squares technique or historical data
**Signal not detected by least squares technique
***Signal falls between two closely spaced frequencies from least squares technique

3.1.3 Comparison with prior ground-based observations

Only one of the previously detected frequencies seem to agree with the TESS data. BPM 30551 has a TESS magnitude of 15.81, which is the dimmest of the target stars and approaches the limiting magnitudes expected for useful asteroseismic data from TESS.

As mentioned in Section 1.2.3, the bandpass of TESS runs through the red to the near-infrared end of the electromagnetic spectrum, whereas the photomultiplier tubes (PMTs) are more sensitive to the bluer end of the visible light portion of the spectrum. Because of this difference in bandpass and the nature of the flux distribution from white dwarfs at T_{eff} near 11000 K, the amplitude of pulsations will be higher in the blue than in the red. A useful scaling for the amplitudes detected at the wavelengths that the TESS bandpass is sensitive to to the wavelengths that PMTs are sensitive to can be found in Kawaler et al. (1994) as Equation 3.3. In the case of TESS (choosing a representative wavelength of roughly 825 nm) compared to the PMTs (choosing a representative wavelength of roughly 425 nm) on a star like BPM 30551 with a temperature of roughly 11260 K according to Fontaine and Brassard (2008), the amplitude seen by TESS should be about 62.2% of that seen at shorter wavelengths. The final column of Table 3.1 represents what the expected amplitude of these signals would be if measured by a PMT rather than the TESS detectors, giving an apples-to-apples comparison against the amplitudes found in ground-based observations.

$$\frac{\delta A_{TESS}}{\delta A_{PMT}} = \frac{\lambda_{PMT}}{\lambda_{TESS}} * \frac{e^{\frac{hc}{kT\lambda_{TESS}}}}{e^{\frac{hc}{kT\lambda_{PMT}}}} * \frac{e^{\frac{hc}{kT\lambda_{PMT}}} - 1}{e^{\frac{hc}{kT\lambda_{TESS}}} - 1} \tag{3.3}$$

It may be that ground-based frequencies are only detectable against the background noise in the case of PMTs which pick up more of the amplitude in objects as hot as white dwarfs. That once again would not seem to explain the detection of numerous new frequencies which would have much larger amplitudes relative to the archived frequencies according to Robinson et al. (1982), which predicted all pulsation frequencies to be effected equally no matter the wavelength of light observed.

The remaining explanation is that the modes of oscillation of this star may have altered over time. Instead, it appears that some modes have been suppressed and new frequencies have emerged.

BPM 30551 is located near the cool-edge (red) of the instability strip, which as addressed in Mukadam et al. (2006), makes it more of a complex pulsator with periods of oscillation generally greater than 600 s and larger amplitudes. This information combined with information from Hermes et al. (2017) about the non-coherence of the pulsation modes indicates that these frequencies of oscillation may be changing significantly over the timescales of months and years. These modes do not maintain their coherence due to stochastic processes similar to those on the Sun knocking the signal out of phase. When the phases of these pulsation modes are not aligned, the frequencies of oscillation expressed by the modes change and cause the irregular shapes and groupings of frequencies seen in the periodogram. Current efforts fit clusters of frequencies to a Lorentzian and use the half-width at half-maximum to describe the frequency's lifetime. This model seems to be able to explain why frequencies associated with periods of over 800 s are only able to exist for timescales of weeks to months before fading and new modes replacing them elsewhere in frequency-space. As it stands, it still remains for models to check how these new sets of frequencies impact the predictions for the different physical properties of the star.

3.2 HE 0532-5605

The DAV HE 0532-5605 is located near the southern ecliptic pole and as a result remains in the observing field of TESS for nearly a year continuously. The star also has a magnitude of roughly 14.94 in the TESS bandpass.

3.2.1 Ground-based behavior

This star's pulsations were discovered by Fontaine et al. (2003) along with MCT 0145-2211 which will be discussed later. HE 0532-5605 was measured for 7040 s at a 40 s sampling time resulting in 176 data points. The two primary periods of oscillation that were identified were near 688.8 and 586.4 s (1451.8 and 1705.3 μHz respectively), but these determinations were limited by the resolution of the data, which was 142 μHz. Fontaine et al. (2003) were able to determine the peaks more precisely by oversampling the data and folding the light curve to provide the best fit.

Castanheira and Kepler (2009) found this star to be near the red edge of the ZZ Ceti instability strip with a $T_{\rm eff} = 11560$ K. Being near the red edge means that it is expected to have complex and long periodic oscillations generally exceeding 600 s. They also claim to have identified numerous other frequencies from the data collected by Fontaine et al. (2003), which have been listed in Table 3.2 for completeness. The most recent observations of HE 0532-5605 came from Kilkenny et al. (2013) to test the Berkeley Visual Imaging Tube detector and lasted for roughly 3000 s with 0.1 s integration times. They detected periods of 438, 707, and 1380 s (720, 1410, and 2280 μHz respectively) and indicated that they believed that the periodicity around 1410 μHz may be unstable and related to the peak originally detected by Fontaine et al. (2003).

Table 3.2 Frequencies of oscillation for HE 0532-5605 from Castanheira and Kepler (2009)

Mode (s)	**Frequency (μHz)**	**Amp (mma)**
522.4	1914.2	2.1
563.7	1774.0	2.5
599.7	1666.7	2.5
686.1	1457.5	5.5
723.7	1381.8	7.8
753.8	1326.6	4.8
822.3	1216.1	3.4
881.7	1134.2	2.9

3.2.2 TESS results

HE 0532-5605 offered the unique opportunity to examine the effects of multiple sectors of data on results. For this study, the first four sectors of TESS data have been applied to act as a proof of concept for studies of future stars. Figures 3.7 and 3.8 show a sample target pixel file from Sectors 2 and 3 respectively. After inspection, only the pipeline mask for Sector 3 required correction, likely due to the extremely bright neighboring star. The pipeline mask had simply been offset by a pixel from the target.

After correcting for this, each of the individual light curves were trimmed to remove non-signal events, most commonly the Earth shining past the telescope's Sun-shade as the instrument

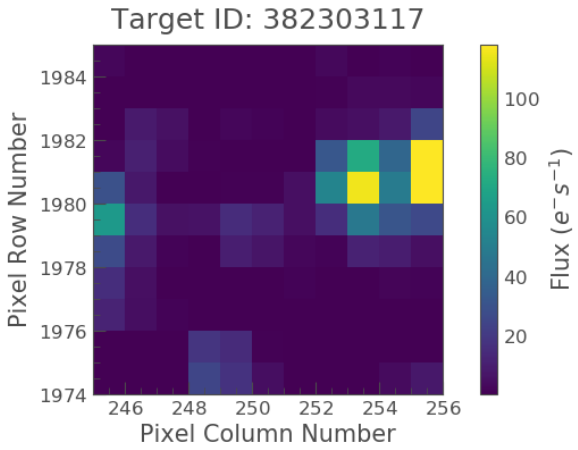

Figure 3.7 The target pixel file of HE 0532-5605 from Sector 2. There is a brighter source nearby, but it does not completely outshine the target which is the central four pixels.

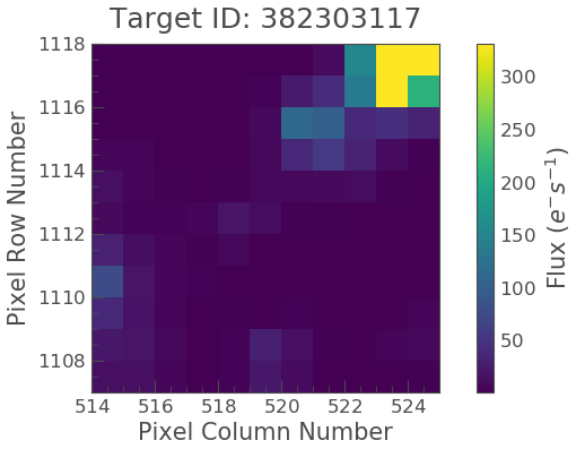

Figure 3.8 The target pixel file of HE 0532-5605 from Sector 3. Examining the color scale, it is clear that the source in the upper right corner is contributing most of the flux for the postage stamp and may hamper the results from that light curve.

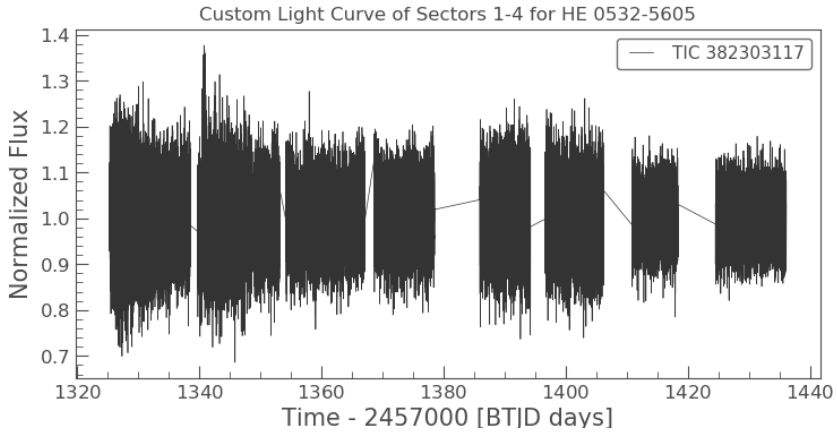

Figure 3.9 The light curve of Sectors 1-4 stitched together for HE 0532-5605. There were greater variations in the flux in the first two sectors of data compared to the latter two. Whether or not this is due to the instrument, data reduction, or the star itself requires further research using more sectors of data.

approached perigee and the corresponding downlink of data as described in the DRNs for Sectors 3 and 4 by Fausnaugh et al. (2019). Each of these light curves are then flattened, sigma-clipped, and normalized such that they can be stitched together to make one longer pseudo-continuous light curve. The resulting light curve has a duty cycle of roughly 74.6% over almost 4 months and can be seen in Figure 3.9. The periodogram that this produces is Figure 3.10. Table 3.3 follows with the identified modes of oscillation produced by this analysis.

Table 3.3 Frequencies of oscillation in multi-sector data of HE 0532-5605.

f (μ**Hz**)	**Alias** (μ**Hz**)	**Sector**	**PSD** ($ppm^2/\mu Hz * 10^7$)	**Amp** (**mma**)	**Temp Corr** (**mma**)
2522.9	5810.4	1	3.399	5.60	8.94
2526.8	5806.5	1	3.266	5.49	8.76
2538.7	5794.6	1	3.125	5.37	8.57
2538.8	5794.5	1-4	3.084	2.91	4.65

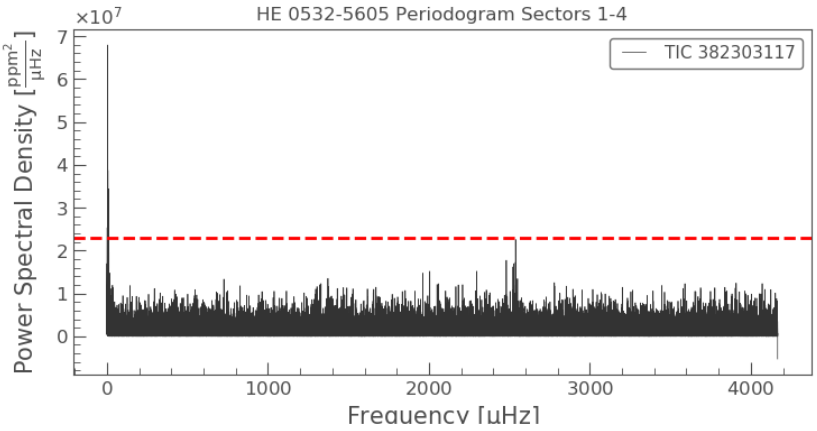

Figure 3.10 The periodogram of Sectors 1-4 stitched together for HE 0532-5605 before correction for attenuation near the Nyquist frequency. None of the peaks seem to be particularly high in amplitude, but there seems to be a possible signal at 2538.8 μHz.

3.2.3 Multi-sector issues

As could clearly be seen in Figure 3.10 and Table 3.3, there were no strong periodicities present. The star seems to vary in brightness significantly more during the first two sectors of observation than the latter two. This could be due to physical differences in the star; for instance, if it were an outburster as described by Bell et al. (2015), the large, brief increase in flux and the low frequency signals may be explained. These outbursts, seen in some cool DAVs reoccur on the time scales of a few weeks, and last a significant fraction of a day. The process of stitching sectors together needs further refinement to reduce noise and not interfere with signals that may be shared between sectors. This would involve backing the direct flux measurements out of the target pixel files, rather than the normalized flux products produced by the `Lightkurve` package. To see the results of analyzing individual sectors of data for this target, refer to Appendix B. Elements of particular interest in Appendix B are the varying signals at low frequency from sector to sector, indicating that the outburster hypothesis has not been ruled out. Together, those signals all appear to be part of the noise, but when evaluated individually, they stand out more clearly.

3.3 MCT 0145-2211

MCT 0145-2211 is located in Sector 3 of the TESS observation field near an edge of one of the CCDs. The star has a magnitude of roughly 15.74 in the TESS bandpass, making it another dim target upon which TESS's capabilities can be tested.

3.3.1 Ground-based behavior

The pulsating behavior of the DAV MCT 0145-2211 was published concurrently with HE 0532-5605 in Fontaine et al. (2003). It was observed over two concurrent evenings for 3740 s on the first and 5780 s on the second, each with sampling times of 10 s. Their observations are listed in Table 3.4. Further periods could likely be resolved with longer observations. They determined the temperature of the star to be around 11550 K, making this another example of a DAV near the red edge of the instability strip.

These observations were followed up by Kilkenny et al. (2013), resulting in Table 3.5. They observed for 50 min with a sampling time of 0.1 s. Note the differences between the two studies over the span of a decade seems to continue to support the claim that DAVs near the red edge of the instability strip change their frequencies of oscillation significantly over time.

Table 3.4 Frequencies of oscillation for MCT 0145-2211 from Fontaine et al. (2003)

Mode (s)	**Frequency (μHz)**	**Amp (mma)***
462.2	2163.6	25
727.9	1373.8	19
823.2	1214.8	17

*Amplitudes from Mukadam et al. (2006)

Table 3.5 Frequencies of oscillation for MCT 0145-2211 from Kilkenny et al. (2013)

Mode (s)	**Frequency (μHz)**	**Amp (mma)***
437	2288.3	10
454	2202.6	7
730	1369.9	6

*Amplitudes approximated from their figures

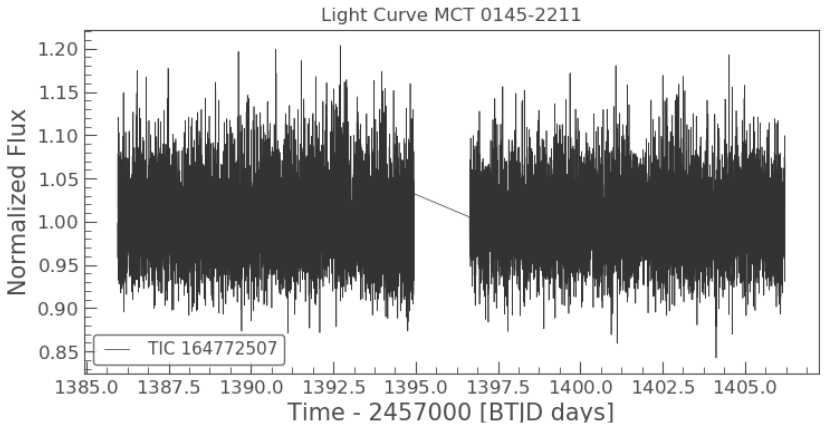

Figure 3.11 The light curve for MCT 0145-2211 after completing all data reduction including some trimming preceding the downlink due to Earth rising over the sunshade on the telescope.

3.3.2 TESS results in comparison

Sector 3 science data were delayed at the start of the run and cut off early near the end of the run to perform tests on the spacecraft's pointing stability, so this is the shortest data set to work with at 20.4 days (with a gap in the middle). The result can be found in Figure 3.11 and the periodogram is shown in Figure 3.12.

The duty cycle is 89.3%, so the window function remains the primary producer of these side lobes which appear roughly 0.8 μHz away from the true signal, which is visible in Figure 3.13. The list of identified frequencies and their associated power spectral densities is found in Table 3.6. An interesting finding in the periodogram produced by this DAV is the unusual shape of the peaks produced by some of the signals. Rather than simply appearing as the square of a *sinc* function as seen for the previous stars, where the width was determined by the run length of the data set and the amplitude was a result of the strength of the signal, many of the peaks in this periodogram take somewhat irregular forms as seen in Figure 3.14.

This is likely due to either very closely spaced modes of oscillation causing *sinc* functions to overlap and deform the original shape, or possibly a signal of frequency exceeding the Nyquist creating an alias that happens to reflect back across the Nyquist frequency and creates an alias

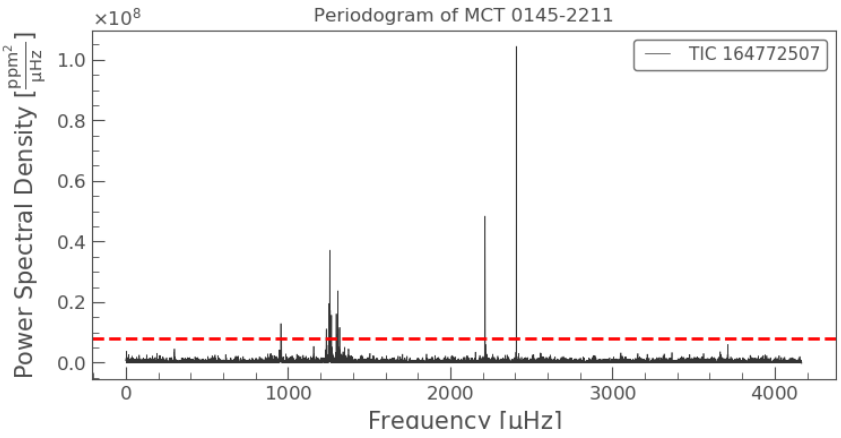

Figure 3.12 The periodogram of MCT 0145-2211.

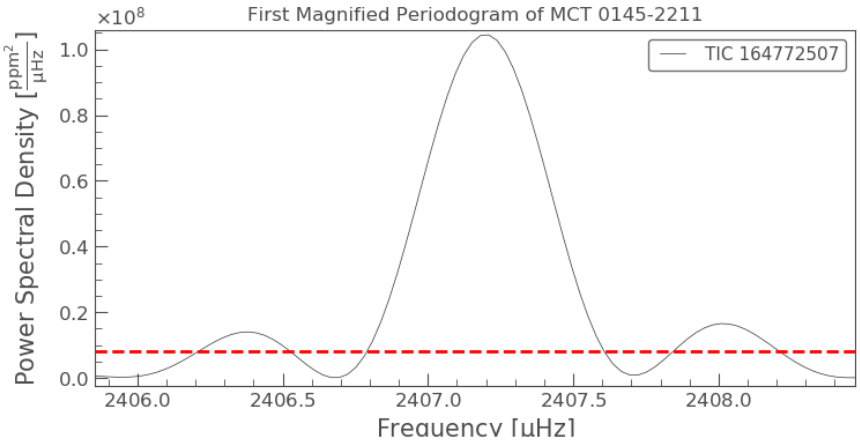

Figure 3.13 The signal at 2407.2 μHz in the periodogram of MCT 0145-2211. This shows the effect of the window function on the target star.

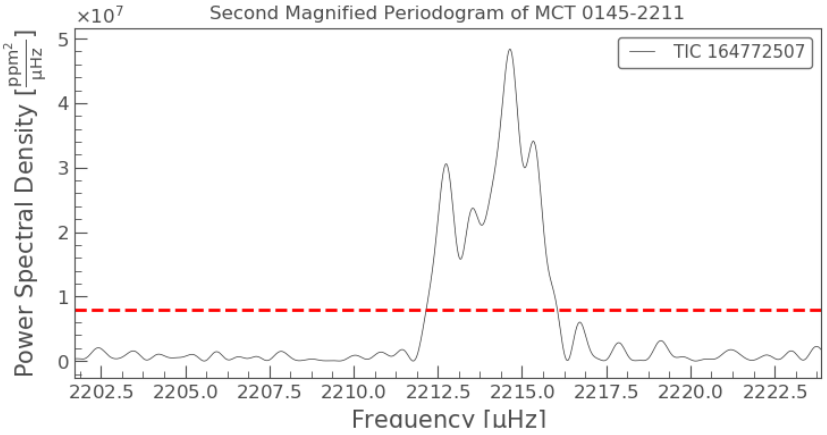

Figure 3.14 The unusual shape of some of the peaks in the periodogram of MCT 0145-2211. This is possibly due to other similar frequencies also producing a signal and blending together, or it could be the result of a short-timescale perturbation in the phase of the mode, such as stochastic input of energy by convection - much as we see in solar-type stars.

very close to an already existing frequency. The second option is in theory possible, but is unlikely because MCT 0145-2211 so closely matches the description of a DAV near the red edge of the instability strip in every other way. Most of the frequencies (including the discovery data and other ground-based observations) are of long period, and those frequencies of oscillation tend to have a very high amplitude.

As seen in Table 3.6, only one of the identified frequencies (2214.6 μHz) seem to roughly match up with the ground-based data, as has been the case for the other cool DAVs discussed. The fact that the signals are so different on a target with data as clean as this supports the claim that DAVs near the red edge of the instability strip are subject to stochastic excitation and deexcitation on short time scales, with modes growing and decaying on months-to-years time scales.

3.4 Conclusions

Studying these three relatively cool DAVs has shown some intriguing results. While TESS data did indicate oscillations in all three stars, the results differed from the prior observed frequencies

Table 3.6 Frequencies of oscillation in MCT 0145-2211.

f (μHz)	Alias (μHz)	PSD ($ppm^2/\mu Hz * 10^7$)	Amp (mma)	LS Amp (mma)	Temp Corr (mma)
955.9	7377.4	1.34	4.14	4.450	6.61
1235.9*	7097.4	1.94	3.90	n/a	6.22
1253.1*	7080.3	2.13	5.21	n/a	8.32
1257.5**	7075.8	4.00	7.13	8.012/6.273	11.39
1260.1*	7073.2	1.89	4.90	n/a	7.82
1264.5*	7068.8	1.26	4.01	n/a	6.40
1267.9*	7065.4	1.70	4.64	n/a	7.41
1297.6	7035.7	1.75	4.71	5.264	7.52
1306.1	7027.2	1.51	4.38	5.801	6.99
1308.8*	7024.5	1.21	3.91	n/a	6.25
1318.0*	7015.3	1.26	4.00	n/a	6.39
2212.7**	6120.6	3.88	7.02	7.830/7.501	11.22
2214.6**	6118.7	6.14	8.83	10.18/10.47	14.11
2407.2	5926.1	1.39	13.3	12.74	21.25

*Signal not detected by least squares technique

**Signal falls between two closely spaced frequencies from least squares technique

of oscillation. The fact that the HE 0532-5605 data seemed to produce significantly different periodograms from sector to sector as seen in Appendix B seemed to indicate that the frequencies of DAVs near the cool edge of the instability strip could vary rapidly over time. This was the noisiest set of data of the three, so follow-up observations may be appropriate using an instrument with a larger aperture to test this hypothesis. The most consistent feature among all of the sectors of HE 0532-5605 data was the comparatively strong signals at low frequency.

All three of the stars seemed to fit the prototype of DAV stars on the cool edge of the instability strip with complex pulsation spectra, characterized by long period pulsations of high amplitude and frequencies that fall within a Lorentzian envelope rather than showing narrow peaks characteristic of coherent pulsation as described by Hermes et al. (2017). This ultimately demonstrates the effective use of TESS photometry to identify new and closely spaced pulsation modes for use in asteroseismic models.

CHAPTER 4. ROSS 548 (AKA ZZ CETI)

Ross 548 was the third identified white dwarf pulsator. The discovery was published by Lasker and Hesser (1971) who identified a primary and secondary mode of oscillation. The primary mode had a period of 212.864 s (4697.8 μHz) and the secondary had a period of 273.0 s (3663 μHz). This has been one of the most commonly measured DAVs in the night sky by other ground-based observers. The star has a temperature in excess of 12000 K, with the most recent observations placing it at 12300 K by Bognar and Sodor (2016), leaving it close to the blue edge of the DAV instability strip. The paper by Bognar and Sodor (2016) also listed the different measurements of the periods and amplitudes of the different identified modes by the follow-up investigations to Lasker and Hesser (1971). The periods and amplitudes are given in Tables 4.1 & 4.2 along with their sources and a weighted average of the amplitudes for the highest amplitude modes are in Table 4.3. The lifetimes of pulsation periods of Ross 548 are remarkably stable for long timescales when compared to the findings from Chapter 3. This makes Ross 548 an ideal target to calibrate TESS, because the highest amplitude peaks should occur at the same frequencies.

Table 4.1 Prior determinations of periodicities in Ross 548 and associated frequencies & amplitudes in the sub-Nyquist regime for TESS.

Period (s)	**Frequency (μHz)**	**Amp (mma)**	**Source**
336.2	2974.4	3	Mukadam et al. (2013)
335.3	2982.4	0.3	Mukadam et al. (2013)
334.5	2989.5	0.3	Mukadam et al. (2013)
333.6	2997.6	0.6	Mukadam et al. (2003)
333.6	2997.6	1.3	Castanheira and Kepler (2009)
333.6	2997.6	0.6	Mukadam et al. (2013)
333.6	2997.6	0.6	Giammichele et al. (2015)
333	3003	1	Kepler et al. (1995)
320	3125	1	Kepler et al. (1995)
319.2	3132.8	0.4	Mukadam et al. (2013)
318.8	3136.8	0.3	Giammichele et al. (2015)
318.1	3143.7	0.9	Mukadam et al. (2003)
318.1	3143.7	1.1	Castanheira and Kepler (2009)
318.1	3143.7	0.4	Mukadam et al. (2013)
318.1	3143.7	0.7	Giammichele et al. (2015)
317.0	3154.6	0.4	Mukadam et al. (2013)
274.8	3639.0	3.4	R.J. Stover and Nather (1977)
274.8	3639.0	3.4	Stover et al. (1980)
274.8	3639.0	1.3	Kepler et al. (1995)
274.8	3639.0	2.9	Mukadam et al. (2003)
274.8	3639.0	3.146	Mukadam et al. (2013)
274.8	3639.0	3.107	Giammichele et al. (2015)
274.5	3643.0	3.5	Castanheira and Kepler (2009)
274.5	3643.0	0.7	Mukadam et al. (2013)
274.5	3643.0	1.2	Giammichele et al. (2015)
274.3	3645.6	5.3	R.J. Stover and Nather (1977)
274.3	3645.6	4.9	Stover et al. (1980)
274.3	3645.6	2.2	Kepler et al. (1995)
274.3	3645.6	4.1	Mukadam et al. (2003)
274.3	3645.6	4.129	Mukadam et al. (2013)
274.3	3645.6	4.299	Giammichele et al. (2015)
273	3663	2-11	Lasker and Hesser (1971)

Table 4.2 Prior determinations of periodicities in Ross 548 and associated frequencies & amplitudes in the super-Nyquist regime for TESS.

Period (s)	**Frequency (μHz)**	**Amp (mma)**	**Source**
217.8	4591.4	0.3	Giammichele et al. (2015)
213.1	4692.6	7.9	R.J. Stover and Nather (1977)
213.1	4692.6	7.7	Stover et al. (1980)
213.1	4692.6	3.3	Kepler et al. (1995)
213.1	4692.6	6.7	Mukadam et al. (2003)
213.1	4692.6	6.587	Mukadam et al. (2013)
213.1	4692.6	6.578	Giammichele et al. (2015)
213.0	4694.8	5.4	Castanheira and Kepler (2009)
213.0	4694.8	1	Mukadam et al. (2013)
212.9	4697.0	2-11	Lasker and Hesser (1971)
212.9	4697.0	1.4	Giammichele et al. (2015)
212.8	4699.2	4.7	R.J. Stover and Nather (1977)
212.8	4699.2	4.4	Stover et al. (1980)
212.8	4699.2	2.1	Kepler et al. (1995)
212.8	4699.2	4.1	Mukadam et al. (2003)
212.8	4699.2	4.293	Mukadam et al. (2013)
212.8	4699.2	4.105	Giammichele et al. (2015)
187.3	5339.0	0.9	Mukadam et al. (2003)
187.3	5339.0	0.9	Castanheira and Kepler (2009)
187	5347.6	1	Kepler et al. (1995)
186.9	5350.5	0.5	Mukadam et al. (2013)
186.9	5350.5	0.9	Giammichele et al. (2015)
186.7	5356.2	0.4	Mukadam et al. (2013)
186.5	5361.9	0.3	Mukadam et al. (2013)

4.1 Period variation of oscillations over time

As one of the most stable DAV pulsators, ZZ Ceti has some of the most extensive data collected reaching back to 1970. Mukadam et al. (2013) analyzed over forty years of data to examine how a pulsation period may change over time. Constraining that rate, which is directly tied to the rate of cooling, has important implications for asteroseismology and astrophysics at large. The frequencies are expected to decrease over time as the degeneracy boundary deepens with the star's cooling,

Table 4.3 Weighted amplitudes of strongest frequencies of pulsation from ground-based observations

Period (s)	**Frequency (μHz)**	**Weighted Amp (mma)**
212.8	4699.2	4.28 ± 0.04
213.1	4692.6	6.86 ± 0.04
274.3	3645.6	4.41 ± 0.04
274.8	3639.0	3.17 ± 0.04

though any residual contraction of the star would lead to frequencies increasing with time. The amount of gravitational contraction is very small in the particular temperature range of DAVs, so the periods of oscillation are generally expected to increase.

In Mukadam et al. (2013), this rate of cooling was determined to change the period of oscillation of the peak associated with the 213.13 s period by a rate of $5.5 * 10^{-15} s/s$. This slow rate seems like it should not be measurable given the resolution of even TESS would be 0.57μHz. For a sense of scale, there are over $10^9 s$ over 40 years, so the sensitivity to measuring the pulsation period would have to be able to detect a change as small as 6-7 μs over 40 years. TESS, on the other hand, would only be able to resolve down to the nearest tens of milliseconds for that oscillation period.

Mukadam et al. (2013) were able to get around that limitation by applying a direct nonlinear least squares fit with variable periods to all of the data from 1970 to 2012 at the same time, greatly improving the resolution. They were also able to verify those results by comparing the observed phase (O) of the peaks to the calculated phase (C) of the peaks when assuming a constant period (P). Plotting the difference in those phases against the epoch (E, the cycle count) allowed for the determination of dP/dt using a best fit of the decades of data for each peak and Equation 4.1 from Mukadam et al. (2013).

$$O - C = \Delta E_0 + E\Delta P + \frac{1}{2} P \frac{dP}{dt} E^2 \tag{4.1}$$

The analysis by Mukadam et al. (2013) was able to extract the rotational and magnetic splitting of different modes of oscillation offering measurements of the rotation rate and magnetic field by

looking at the spacing of different multiplets. All of the tools implemented by Mukadam et al. (2013) together produce a reliable measure of the evolutionary cooling rate that can be used to determine the core composition of the star, a possible constraint on the mass of axions, and place constraints on the age of the galaxy when using white dwarfs as clocks.

This analysis hinges upon the star having very stable oscillation frequencies, amplitudes, and phases - all of which could be subject to shorter-timescale changes through interaction with the convection zone or small-scale magnetic cycles. Thus, we expect that Ross 548 would be a good "calibration source" to see if the amplitudes and frequencies measured by TESS are consistent with those found by forty years of ground-based studies.

4.2 TESS results

Most of the data reduction for ZZ Ceti was provided as an example in Chapter 2. ZZ Ceti was located in Sector 3, so it was subject to the same issues in data collection as MCT 0145-2211. More data needed to be trimmed in the case of ZZ Ceti because the Earth rising beyond the sunshade seemed to impact it sooner. This resulted in a duty cycle of approximately 84.9%, which was still high and should not significantly impair the signals compared to the natural window function of the observation. It was also located near some sources of similar brightness, but the mask provided by the pipeline avoided any contaminated pixels as seen in Figure 2.4. The identified frequencies and their corresponding aliases, attenuated power spectra, amplitudes, and temperature corrections are included in Table 4.4. The table also includes amplitudes obtained via least squares fitting which was then corrected for attenuation and temperature and the mean ground-based amplitudes from Table 4.3.

4.2.1 Alias issue

As seen in Table 4.4, the frequencies of each signal and their aliases are similar. Consequently, I relied on the ground-based observations to determine which frequencies in the periodogram were produced by aliasing across the Nyquist frequency and which were produced by a mode of oscillation.

Table 4.4 Frequencies of oscillation in TESS data on Ross 548 (ZZ Ceti).

f (μHz)	Alias (μHz)	PSD ($\frac{ppm^2}{\mu Hz} * 10^6$)	Amp (mma)	Temp Corr (mma)	LS Amp (mma)	Ground-based Mean (mma)
5.6	8327.7	1.00	2.179	3.43	n/a	n/a
3633.4*	4699.9	5.85**	2.59	4.07	3.64	4.28 $\pm$ 0.04
3639.4	4693.9	3.53	2.01	3.16	3.88	3.17 $\pm$ 0.04
3641.4*	4691.9	13.57**	3.93	6.18	6.95	6.86 $\pm$ 0.04
3646.3	4687.0	6.05	2.64	4.14	4.15	4.41 $\pm$ 0.04

*Super-Nyquist frequency matches ground-based data, indicating the super-Nyquist is actually the real signal.

**Applied the attenuation factor for the true frequency rather than the sub-Nyquist alias.

This is particularly challenging in this case because ZZ Ceti is a DAV near the blue edge of the instability strip, which leaves it more likely to possess short period (less than 600 s) modes of oscillation. The modes of oscillation for ZZ Ceti nearly overlap across the Nyquist frequency of TESS data, so it was difficult to separate out the amplitude caused by the primary peaks of the signals from the amplitudes contributed from the side lobes of others. Figure 4.1 shows the effects of multiple clear peaks interfering with each other due to Nyquist aliasing. The cleanest way to remove these effects was via a least squares analysis that fit the profile of a sinusoid oscillating at given frequency and phase, and then subtracted the effect of that sinusoid from the periodogram as seen in the second to last column of Table 4.4.

4.3 Conclusions

The TESS data accurately reflected the presence of the largest peaks detected in ground-based photometry. The amplitudes of each signal were extracted both via least squares analysis and the Lomb-Scargle periodograms produced by `Lightkurve` despite aliasing across the Nyquist frequency causing some blending of the signal. These amplitudes had varying degrees of agreement with the mean of the ground-based observations, indicating that more work may need to be done to reliably determine the amplitudes of pulsation modes for other DAVs in future studies. In most cases the amplitudes obtained via the Lomb-Scargle periodograms produced by `Lightkurve` agreed within

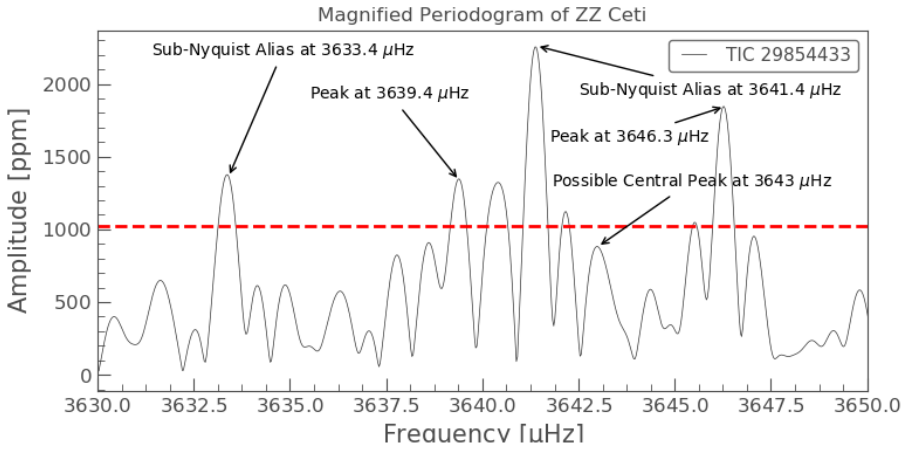

Figure 4.1 This magnified version of the periodogram of ZZ Ceti demonstrates the overlapping aliases and real signals. Some of the lower amplitude central peaks of the multiplets discussed by Mukadam et al. (2013) also appear to be present but below the established significance threshold.

roughly 10% of the ground-based mean measurements after correcting for attenuation due to the Nyquist frequency and the difference in bandpass. The measurements via this method seemed to under-measure, though the degree of under-measurement varied from mode to mode. Future studies will require further observations to more tightly constrain the differences between the TESS data and the average of ground-based data. Confirmation of the well-established frequencies of observation provides proof that TESS is able to expand upon the previous work of ground-based astronomy and should be able to discover more DAVs that can be used to better our understanding of white dwarfs.

CHAPTER 5. SUMMARY AND DISCUSSION

5.1 TESS successes

In this work, I determined that TESS could successfully identify the modes of oscillation for white dwarf pulsators despite the fact that many of the pulsators examined were more than two magnitudes dimmer than the types of targets TESS was designed to look for. I also demonstrated that multiple sectors of TESS data can be stitched together to produce usable results, albeit this should be followed up with studies on targets with modes of variability with longer lifetimes.

5.2 Results for the four DAV pulsators

5.2.1 BPM 30551

When comparing BPM 30551's ground-based data to the results from TESS, the identified frequencies from TESS did not align with the prior results. That said, the frequencies are expected to change over the decades since this star was last observed with careful photometric instruments. The work with TESS verified numerous new frequencies of oscillation that may be able to be backed up with ground-based observations, though they are likely to have already changed due to the short lifetimes of modes of oscillation for DAVs on the cool edge of the instability strip. This star's power spectrum also supported the theory that DAVs near the cool edge of the instability strip tend to have more complex and high amplitude oscillations with long periods. These frequencies of oscillation are often due to incoherent modes that are randomly knocked in and out of phase, much like the processes on the Sun.

5.2.2 HE 0532-5605

Through the analysis of this star over multiple sectors of data, I was able to somewhat successfully identify a few frequencies of oscillation, though it seems that HE 0532-5605 currently has no high amplitude frequencies of oscillation. This star also demonstrated the limits of what examining multiple sectors of data at the same time can do due to its varying low frequency signals as seen in Appendix B. When inspecting all four sectors together, the low frequency end of the periodogram looks like pure noise; however, if observed sector by sector, it appears that there may be some low frequency signals in this star that are varying over time. This was another example of a star near the red edge of the instability strip changing over time, possibly exhibiting outbursting behavior. Follow-up studies of this star may be able to confirm its outbursting behavior if observed for an extended period of time (roughly a month) with an instrument of higher resolution than TESS.

5.2.3 MCT 0145-2211

This cool-edge DAV had the most numerous identifiable peaks of those in this study with many at high amplitudes. As with the others, those modes did not seem to match up with the frequencies identified by prior terrestrial observations. Even so, it remained self-consistent with expectations for DAVs approaching the red edge of the instability strip due to its high amplitude peaks detected at frequencies generally greater than 600 s. The most distinguishing feature of this data set was the irregularly shaped peaks at numerous points in the power spectrum. These are likely formed by incoherent modes of oscillation that are stochastically kicked out of phase and gradually settle back down, just as discussed with BPM 30551.

5.2.4 Ross 548 (ZZ Ceti)

This was the only blue edge DAV studied in this paper, but it did confirm that TESS will be able to detect long-lifetime modes of oscillation in DAVs. Each of the major modes of oscillation were detected where they were expected to appear despite needing to navigate aliased high frequency signals. The relative amplitudes of those frequencies was also preserved within reasonable agreement

with ground-based data, but further work will need to be done to get the amplitudes to match up more precisely. There also existed some evidence of the lower amplitude central peaks of the two multiplets in the TESS data, though they fell below the significance threshold. Further examination of the star would have decreased the noise in the data and could confirm the existence of these peaks. The work on this star also demonstrated differences between the amplitudes inferred by the Lomb-Scargle periodograms employed by `Lightkurve` and the least squares analysis employed in previous studies. Future work will need to be done to determine what is causing these differences.

5.3 Future prospects

For upcoming projects, it is essential to test the method of combining sectors of data on a more consistent pulsator than HE 0532-5605. Its possible outbursting behavior makes the low frequency end of the periodogram naturally high in amplitude, which in turn makes it difficult to determine how successful the process is at resolving frequencies. The fact that it is also near the cool edge of the white dwarf instability strip means that it does not have long-lifetime modes that will be present throughout the whole of multiple months of observation.

Another step of this analysis to further develop is improving the uncertainties in the conversion of amplitudes detected by TESS data sets to the amplitudes measured by ground-based counterparts. Currently, a simple conversion factor is applied using Equation 3.3 and two central wavelengths of the bandpass for PMTs and the TESS detectors to account for the inherent difference in flux radiated by a white dwarf at different wavelengths. This process scales the amplitudes of TESS measurements up to within 10% of average ground-based observations, but does not align all frequencies with ground-based measurements by the same amount at this time. Further observations are required to determine the source of this discrepancy.

Lastly, the sampling time of TESS at two minutes is inconvenient, particularly for DAVs near the blue edge of the instability strip. This is because the Nyquist frequency is so low that high frequency signals can be mirrored across the Nyquist and can become interwoven with some of the lower frequency signals as was nearly the case with ZZ Ceti. Ground-based observations will need

to follow-up on TESS discoveries to distinguish real frequencies from their aliases because almost none of the TESS DAVs will have been as extensively studied as ZZ Ceti. The DAV candidates that it has discovered will not have ground-based data to sort out the real signals from the aliases of high frequency signals as I was able to do with ZZ Ceti.

5.4 Acknowledgements

This research made use of `Lightkurve`, a Python package for Kepler and TESS data analysis (Lightkurve Collaboration, 2018). The work in this document also would not have been possible without the guidance, patience, support, and advice of my advisor, Dr. Steven Kawaler and the Department of Physics and Astronomy at Iowa State University. Another large thank you goes out to the TESS Asteroseismic Science Consortium (TASC) for building numerous helpful resources and tools that directed my search and narrowed my goals for this research.

BIBLIOGRAPHY

Basu, S. and Chaplin, W. J. (2017). *Asteroseismic Data Analysis Foundations and Techniques*. Princeton University Press, Princeton, New Jersey.

Bell, K. J., Hermes, J. J., Bischoff-Kim, A., Moorhead, S., Montgomery, M. H., Østensen, R., Castanheira, B. G., and Winget, D. E. (2015). KIC 4552982: Outbursts and asteroseismology from the longest pseudo-continuous light curve of A ZZ Ceti. *Astrophysical Journal*, 809(1):14.

Bognar, Z. and Sodor, A. (2016). White Dwarf Period Tables I. Pulsators with hydrogen-dominated atmospheres. *Information Bulletin on Variable Stars*, 6xxx(6184):1–31.

Campante, T. L., Schofield, M., Kuszlewicz, J. S., Bouma, L., Chaplin, W. J., Huber, D., Christensen-Dalsgaard, J., Kjeldsen, H., Bossini, D., North, T. S. H., Appourchaux, T., Latham, D. W., Pepper, J., Ricker, G. R., Stassun, K. G., Vanderspek, R., and Winn, J. N. (2016). The asteroseismic potential of TESS: exoplanet-host stars. *arXiv*, 1608.01138(v1):1–31.

Castanheira, B. G. and Kepler, S. O. (2009). Seismological studies of ZZ Ceti stars - II. Application to the ZZ Ceti class. *Monthly Notices of the Royal Astronomical Society*, 396(3):1709–1731.

Fausnaugh, M., Burke, C., Caldwell, D., Jenkins, J., Smith, J., Twicken, J., Vanderspek, R., Doty, J., Li, J., Ting, E., and Villasenor, J. (2019). TESS Data Release Notes.

Fontaine, G., Bergeron, P., Billeres, M., and Charpinet, S. (2003). A Confirmation of the Optical Spectroscopy Approach: Discovery of Two More Pulsating DA (ZZ Ceti) White Dwarfs. *The Astrophysical Journal*, 591(2):1184–1191.

Fontaine, G. and Brassard, P. (2008). The Pulsating White Dwarf Stars. *Publications of the Astronomical Society of the Pacific*, 120(872):1043–1096.

Giammichele, N., Fontaine, G., Bergeron, P., Brassard, P., Charpinet, S., Pfeiffer, B., and Vauclair, G. (2015). A NEW ANALYSIS of the TWO CLASSICAL ZZ CETI WHITE DWARFS GD 165 and ROSS 548. I. PHOTOMETRY and SPECTROSCOPY. *Astrophysical Journal*, 815(56):1–12.

Gilliland, R. L., Brown, T. M., Christensen-Dalsgaard, J., Kjeldsen, H., Aerts, C., Appourchaux, T., Basu, S., Bedding, T. R., Chaplin, W. J., Cunha, M. S., De Cat, P., De Ridder, J., Guzik, J. A., Handler, G., Kawaler, S., Kiss, L., Kolenberg, K., Kurtz, D. W., Metcalfe, T. S., Monteiro, M. J. P. F. G., Szabó, R., Arentoft, T., Balona, L., Debosscher, J., Elsworth, Y. P., Quirion, P.-O., Stello, D., Suárez, J. C., Borucki, W. J., Jenkins, J. M., Koch, D., Kondo, Y., Latham, D. W., Rowe, J. F., and Steffen, J. H. (2010). Kepler Asteroseismology Program: Introduction and First Results. *Publications of the Astronomical Society of the Pacific*, 122(888):131–143.

Hermes, J. J., Gaensicke, B. T., Kawaler, S. D., Greiss, S., Tremblay, P. E., Fusillo, N. P. G., Raddi, R., Fanale, S. M., Bell, K. J., Dennihy, E., Fuchs, J. T., Dunlap, B. H., Clemens, J. C., Montgomery, M. H., Winget, D. E., Chote, P., Marsh, T. R., and Redfield, S. (2017). White Dwarf Rotation as a Function of Mass and a Dichotomy of Mode Linewidths: Kepler Observations of 27 Pulsating DA White Dwarfs Through K2 Campaign 8. *The Astrophysical Journal Supplemenet Series*, 232(23):1–28.

Hesser, J. E., Lasker, B. M., and Neupert, H. E. (1976). High-frequency stellar oscillations. XI. The ZZ CET star BPM 30551. *The Astrophysical Journal*, 209(3):853–857.

Kawaler, S. D., Bond, H. E., Sherbert, L. E., and Watson, T. K. (1994). High-Speed Hubble Space Telescope ultraviolet photometry of two DB white dwarfs: Nonradial and radial pulsations. *The Astrophysical Journal*, 107(1):298–305.

Kepler, S., Giovannini, O., Costa, A., Winget, D., Nather, R. E., Kanaan, A., Kleinman, S., Marar, T., Ashoka, B., Mahra, H., Solheim, J.-E., Emanuelsen, P.-I., Olsen, ., Meištas, E., Tereshchenko, V., Kardapolov, V., Rspaev, F., Sullivan, D., Wickramasinghe, D., Bessell, M., Wu, K., ODonoghue, D., Buckley, D., Warner, B., Haswell, C., Baptista, R., Neill, D., and Birch, P. (1995). Multisite observations of the DAV white dwarf R 548. *Open Astronomy*, 4(2):238–244.

Kilkenny, D., Welsh, B. Y., Koen, C., Gulbis, A. A., and Kotze, M. M. (2013). A search for p-mode pulsations in white dwarf stars using the Berkeley Visible Imaging Tube detector. *Monthly Notices of the Royal Astronomical Society*, 437(2):1836–1839.

Lasker, B. M. and Hesser, J. E. (1971). High-frequency stellar oscillations. VI. R548, a periodically variable white dwarf. *The Astrophysical Journal*, 163(3):89–93.

Lightkurve Collaboration; Cardoso, José Vinícius de Miranda; Hedges, C. G.-S. M. S. N. C. A. M. B. T. H. O. S. S. T. E. Z. J. T. A. M. K. C. G. (2018). Lightkurve: Kepler and TESS time series analysis in Python.

Mestel, L. (1952). On the theory of white dwarf stars: I. the energy sources of white dwarfs. *Monthly Notices of the Royal Astronomical Society*, 112(6):583–597.

Mukadam, A. S., Bischoff-Kim, A., Fraser, O., Córsico, A. H., Montgomery, M. H., Kepler, S. O., Romero, A. D., Winget, D. E., Hermes, J. J., Riecken, T. S., Kronberg, M. E., Winget, K. I., Falcon, R. E., Chandler, D. W., Kuehne, J. W., Sullivan, D. J., Reaves, D., Von Hippel, T., Mullally, F., Shipman, H., Thompson, S. E., Silvestri, N. M., and Hynes, R. I. (2013). Measuring the evolutionary rate of cooling of zz ceti. *Astrophysical Journal*, 771(17):1–11.

Mukadam, A. S., Kepler, S. O., Winget, D. E., Nather, R. E., Kilic, M., Mullally, F., Von Hippel, T., Kleinman, S. J., Nitta, A., Guzik, J. A., Bradley, P. A., Matthews, J., Sekiguchi, K., Sullivan, D. J., Sullivan, T., Shobbrook, R. R., Birch, P., Jiang, X. J., Xu, D. W., Joshi, S., Ashoka, B. N., Ibbetson, P., Leibowitz, E., Ofek, E. O., Meištas, E. G., Janulis, R., Ališauskas, D., Kalytis, R., Handler, G., Kilkenny, D., O'Donoghue, D., Kurtz, D. W., Müller, M., Moskalik, P., Ogloza,

W., Zola, S., KrzesiŃski, J., Johannessen, F., Gonzalez-Perez, J. M., Solheim, J. E., Silvotti, R., Bernabei, S., Vauclair, G., Dolez, N., Fu, J. N., Chevreton, M., Manteiga, M., Suárez, O., Ulla, A., Cunha, M. S., Metcalfe, T. S., Kanaan, A., Fraga, L., Costa, A. F., Giovannini, O., Fontaine, G., Bergeron, P., O'Brien, M. S., Sanwal, D., Wood, M. A., Ahrens, T. J., Silvestri, N., Klumpe, E. W., Kawaler, S. D., Riddle, R., Reed, M. D., and Watson, T. K. (2003). Constraining the evolution of ZZ Ceti. *Baltic Astronomy*, 12(1):71–103.

Mukadam, A. S., Montgomery, M. H., Winget, D. E., Kepler, S. O., and Clemens, J. C. (2006). Ensemble Characteristics of the ZZ Ceti Stars. *The Astrophysical Journal*, 640(2):956–965.

Nather, R. E., Winget, D., and Clemens, J. (1990). The Whole Earth Telescope: A new astronomical instrument. *The Astrophysical Journal*, 361(1):309–317.

Ricker, G. R., Winn, J. N., Vanderspek, R., Latham, D. W., Bakos, G. A., Bean, J. L., Berta-Thompson, Z. K., Brown, T. M., Buchhave, L., Butler, N. R., Butler, R. P., Chaplin, W. J., Charbonneau, D., Christensen-Dalsgaard, J., Clampin, M., Deming, D., Doty, J., De Lee, N., Dressing, C., Dunham, E. W., Endl, M., Fressin, F., Ge, J., Henning, T., Holman, M. J., Howard, A. W., Ida, S., Jenkins, J., Jernigan, G., Johnson, J. A., Kaltenegger, L., Kawai, N., Kjeldsen, H., Laughlin, G., Levine, A. M., Lin, D., Lissauer, J. J., MacQueen, P., Marcy, G., McCullough, P. R., Morton, T. D., Narita, N., Paegert, M., Palle, E., Pepe, F., Pepper, J., Quirrenbach, A., Rinehart, S. A., Sasselov, D., Sato, B., Seager, S., Sozzetti, A., Stassun, K. G., Sullivan, P., Szentgyorgyi, A., Torres, G., Udry, S., and Villasenor, J. (2014). The Transiting Exoplanet Survey Satellite. *arXiv*.

R.J. Stover, E. R. and Nather, R. E. (1977). New observations of the pulsating white dwarf R548. *Publications of the Astronomical Society of the Pacific*, 89(11):912–918.

Robinson, E. L., Kepler, S. O., and Nather, R. E. (1982). Multicolor variations of the ZZ Ceti stars. *The Astrophysical Journal*, 259(1):219–231.

Scargle, J. D. (1982). Statistical aspects of spectral analysis of unevenly spaced data. *Astrophysical Journal*, 263(2):835–853.

Stover, R. J., Hesser, J. E., Lasker, B. M., Nather, R. E., and Robinson, E. L. (1980). Period stability of the pulsating white dwarf R548 (=ZZ Ceti). *Astrophysical Journal*, 548(2):865–870.

Van Grootel, V., Fontaine, G., Brassard, P., and Dupret, M. A. (2013). The Instability Strip of ZZ Ceti White Dwarfs and Its Extension to the Extremely Low Mass Pulsators. *Progress in Physics of the Sun and Stars: A New Era in Helio- and Asteroseismology. Proceedings of a Fujihara Seminar held 25-29 November*, 479(2012):229–235.

VanderPlas, J. T. (2017). Understanding the Lomb-Scargle Periodogram. *arXiv*, 1703.09824(v1):1–55.

Winget, D., Hansen, C., Liebert, J., Van Horn, H., Fontaine, G., Nather, R., Kepler, S., and Lamb, D. (1987). An independent method for determining the age of the universe. *The Astrophysical Journal*, 315(2):L77–L81.

Winget, D. and Kepler, S. (2008). Pulsating White Dwarf Stars and Precision Asteroseismology. *Annual Review of Astronomy and Astrophysics*, 46(1):157–199.

APPENDIX A. BACKGROUND STARS

These are examples of sample stars from the target pixel file that are not known pulsators and are only related to their host target by similar position in the sky. The main issues to watch out for are the flux from these stars dominating the frame and any signals that seem to persist for all targets on the TPF. If all of the targets share the same signal, it is more likely an artifact of some systematic error in the data pipeline or telescope pointing.

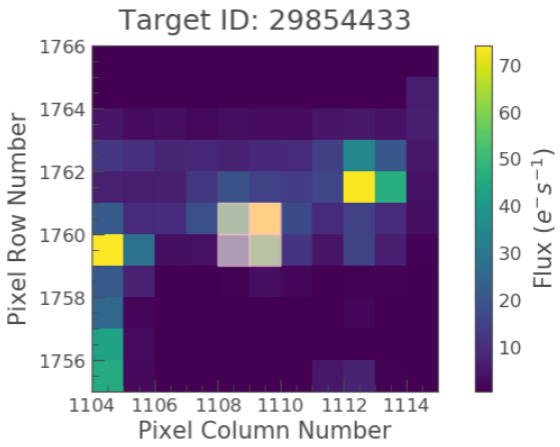

Figure A.1 This is the mask that was used on the DAV ZZ Ceti TPF. Use this as a comparison to nearby stars to see if there are any signals that are shared among these targets.

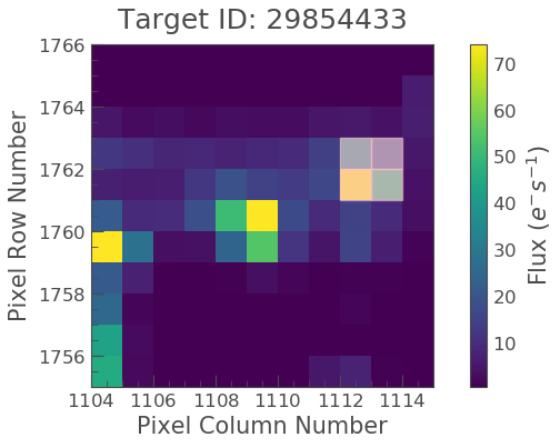

Figure A.2 This is a nearby star roughly 1 arcminute away from ZZ Ceti in the sky that appears to be approximately the same apparent brightness to ZZ Ceti.

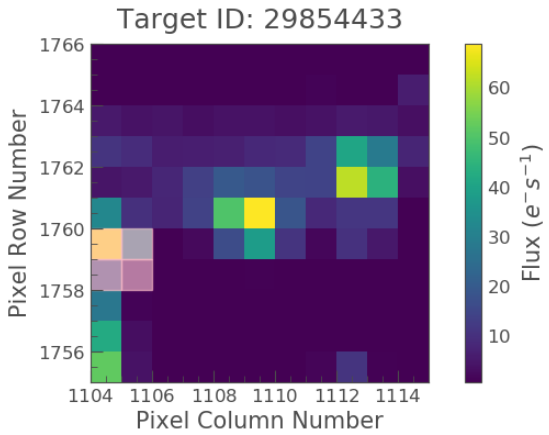

Figure A.3 This is a second nearby star roughly 1 arcminute away from ZZ Ceti in the sky that appears to be approximately the same apparent brightness to ZZ Ceti.

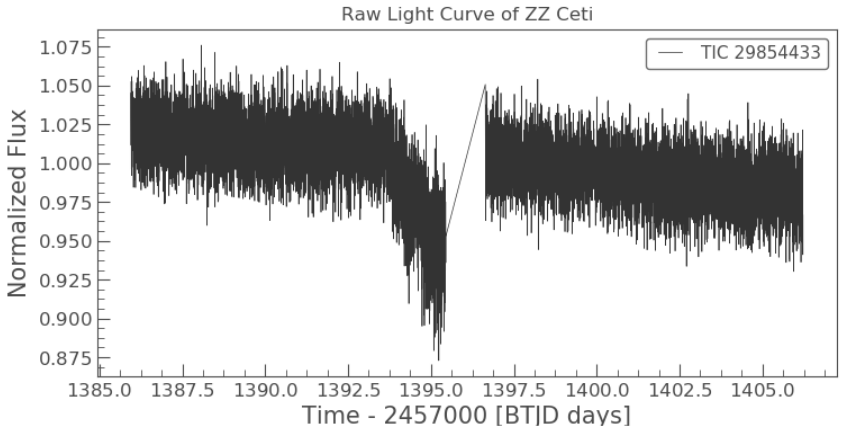

Figure A.4 The raw light curve of ZZ Ceti.

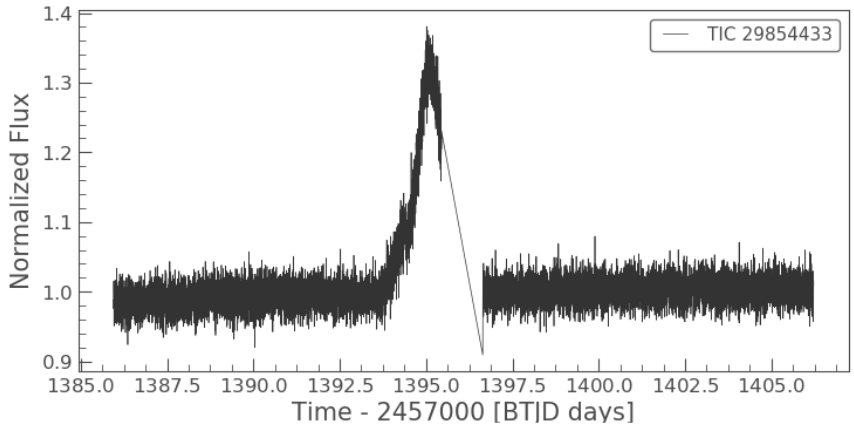

Figure A.5 This is the raw light curve from the first nearby star roughly 1 arcminute away from ZZ Ceti in the sky of approximately the same apparent brightness to ZZ Ceti.

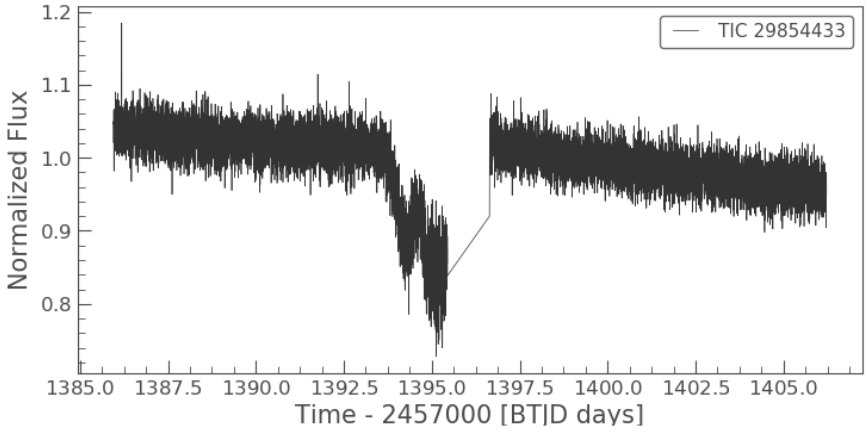

Figure A.6 This is the raw light curve from the second nearby star roughly 1 arcminute away from ZZ Ceti in the sky of approximately the same apparent brightness to ZZ Ceti.

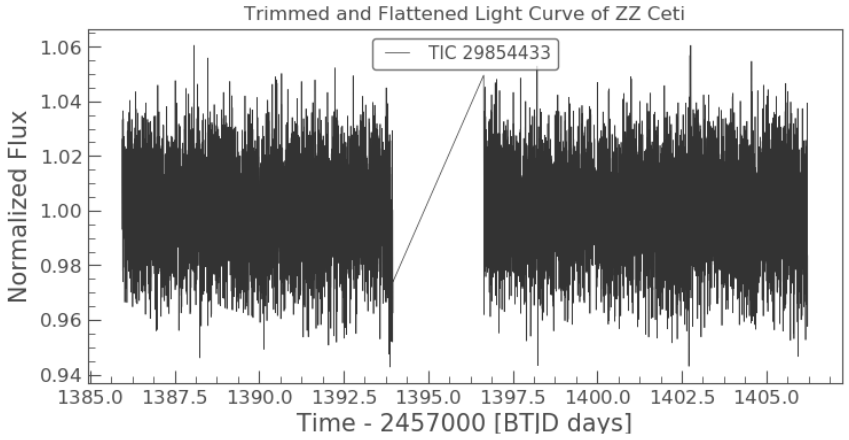

Figure A.7 This is the completely reduced light curve of ZZ Ceti.

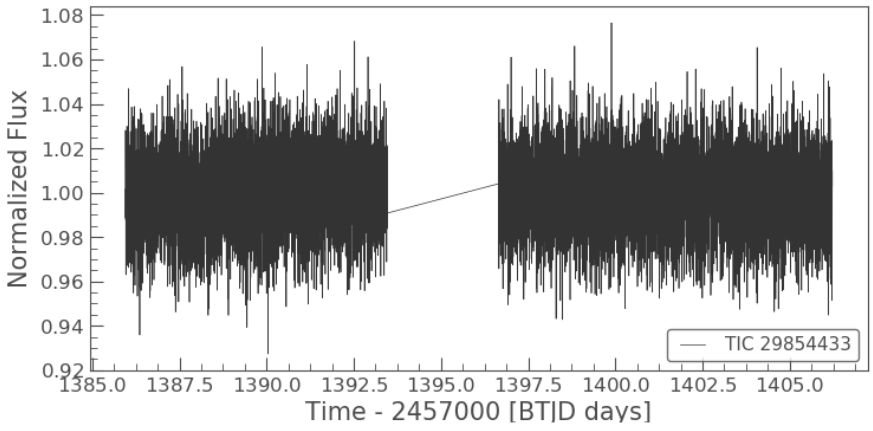

Figure A.8 This is the completely reduced light curve of the first test star near ZZ Ceti using the same methods to keep everything consistent.

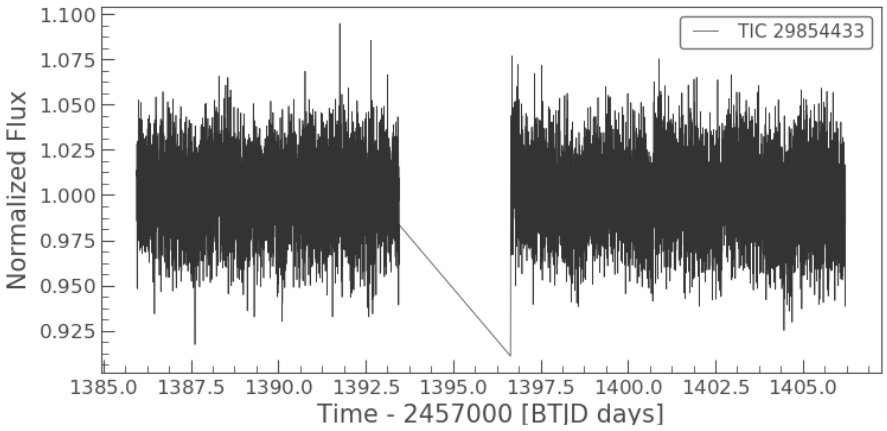

Figure A.9 This is the completely reduced light curve of the second test star near ZZ Ceti using the same methods to keep everything consistent.

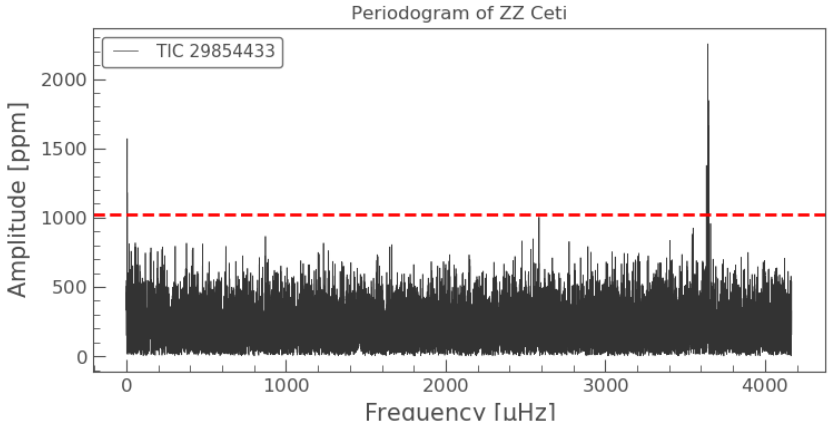

Figure A.10 The Lomb-Scargle periodogram for ZZ Ceti. Compare this to the test stars' periodograms to figure out if there are any signals present in all three that could be caused by systematic errors.

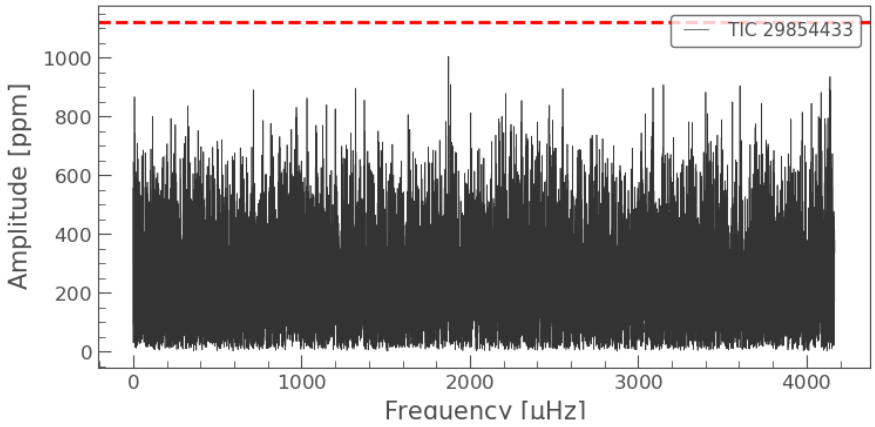

Figure A.11 The Lomb-Scargle periodogram for the first test star near ZZ Ceti. There does not seem to be significant signal that rises above the background noise.

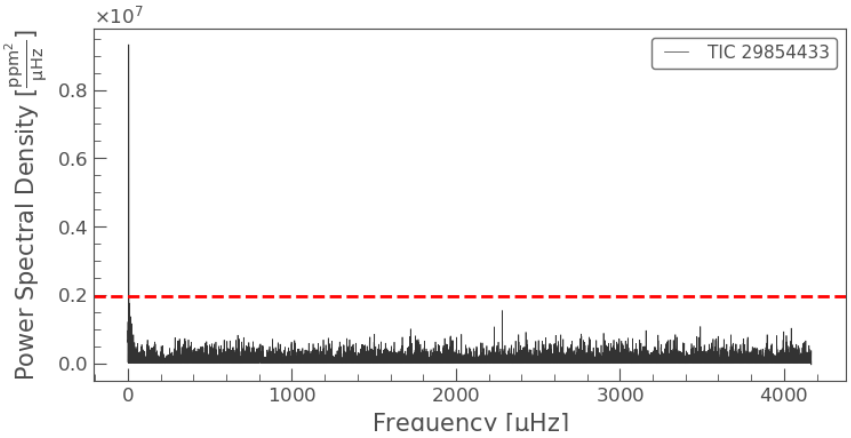

Figure A.12 The Lomb-Scargle periodogram for the second test star near ZZ Ceti. There seems to be a large signal at low frequency that seems to be real. Figure A.14 will follow up on this to compare against the low frequency signal spotted in ZZ Ceti.

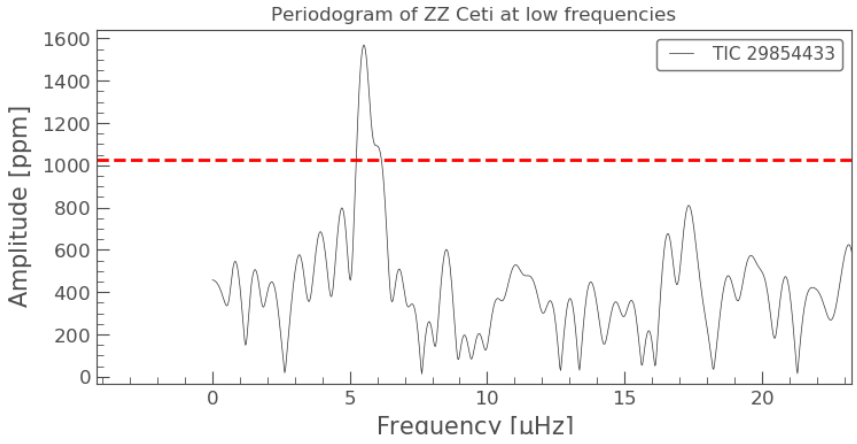

Figure A.13 The Lomb-Scargle periodogram for ZZ Ceti at low frequency where there appears to be a real signal at roughly 5.51 μHz. If this signal is also spotted in the test star, it does seem possible that this could have been an artifact of the data reduction process instead.

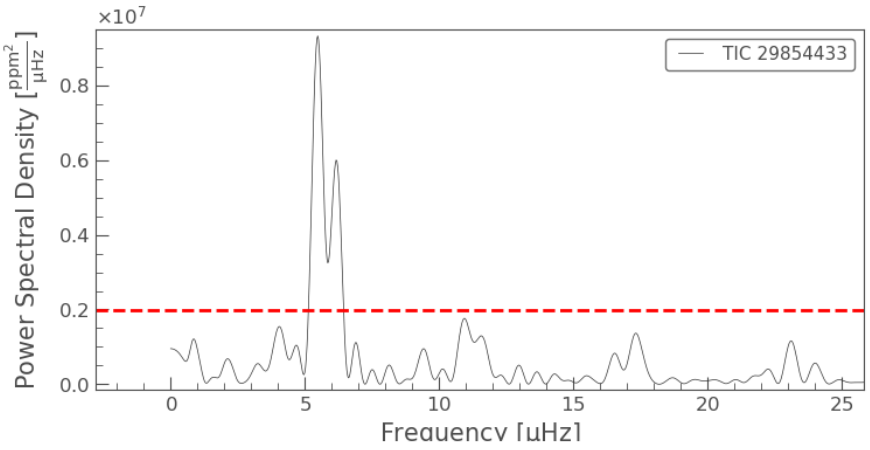

Figure A.14 The Lomb-Scargle periodogram for the second test star near ZZ Ceti at low frequency. There appears to be another large signal at low frequency that seems to be real at roughly 5.48 μHz. This is remarkably close to the signal found in ZZ Ceti, casting doubt on whether or not that signal is real. That said the difference between those two frequencies in period space is roughly 15 minutes, so the fact that they do not line up perfectly does suggest that the signal may be possible. If more data could be collected on this second test star (none was available on MAST at the time of this writing), it could shed further light on the subject.

APPENDIX B. HE 0532-5605 SECTOR LIGHT CURVES AND PERIODOGRAMS

The figures and tables below show the results of examining HE 0532-5605 sector by sector, rather than as a whole. One will notice that even from sector to sector, the frequencies of oscillation seem to vary, making this star of interest for further study to try to detect any sort of pattern in this behavior. The variation in frequencies from sector to sector can also help explain why none of the frequencies produced a strong signal when all of the sectors were stitched together. The low frequency regime has also been focused on due to its variation from sector to sector without the signal seeming to come from purely noise alone.

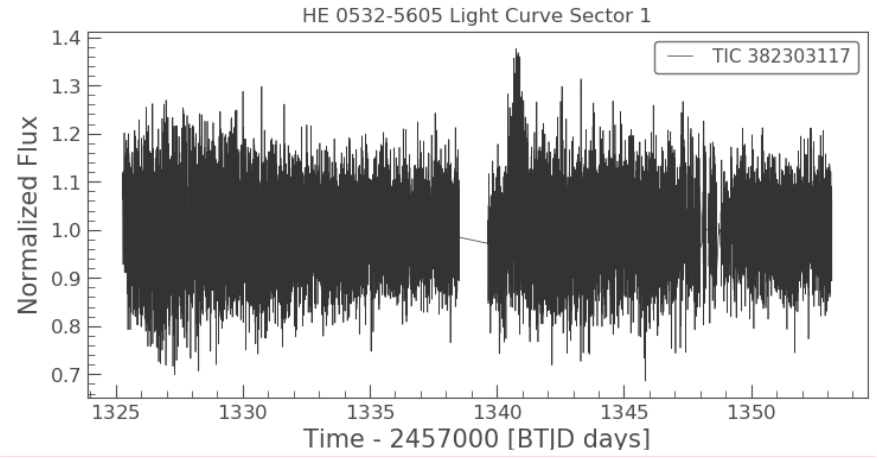

Figure B.1 This is the light curve produced in Sector 1. There seems to be especially large variations in flux from the star despite the fitting of the mask on the target pixel file. This may be due to some uncorrected variable in the data collection for this sector. There seems to be a possible outburst around 1340 days.

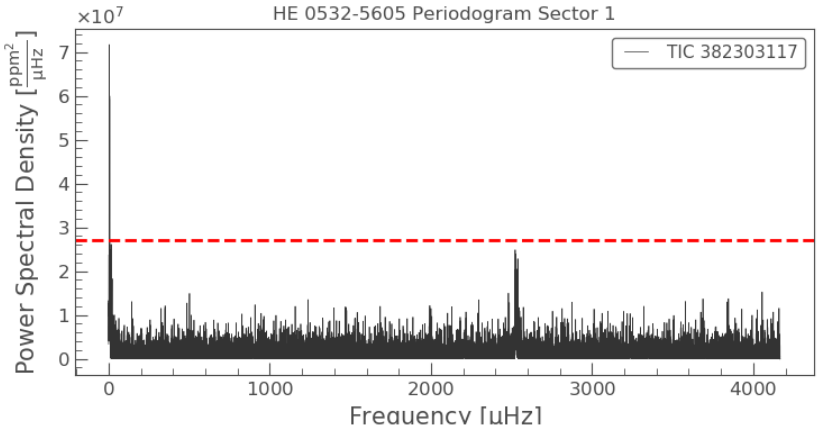

Figure B.2 This is the periodogram for Sector 1. None of the frequencies stand out particularly high above the noise besides at low frequency and maybe 2522.9, 2526.8, and 2538.7 μHz, which do not really agree too closely with archival data.

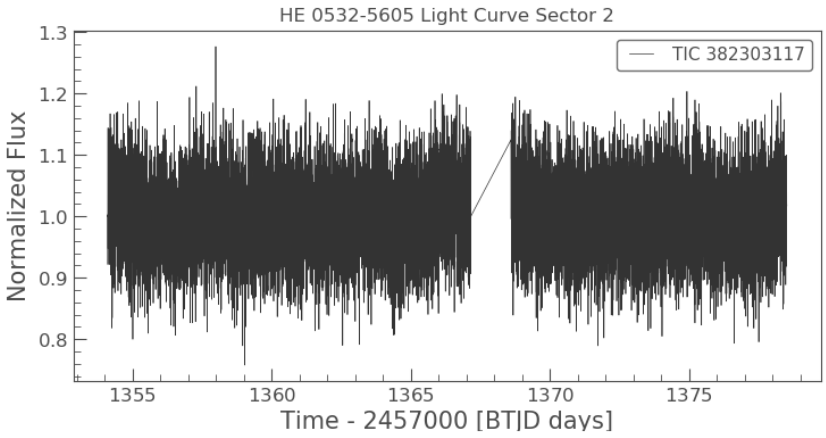

Figure B.3 This is the light curve produced in Sector 2. There still seems to be large variations in flux from the star. This sector has a larger duty cycle than any of the other three.

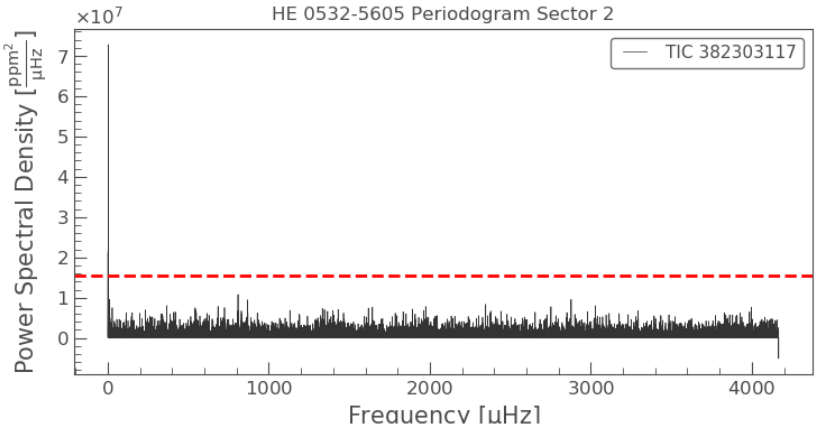

Figure B.4 This is the periodogram for Sector 2. There is extraordinarily high signal coming from the low frequencies despite the reasonably flat light curve. Closer inspection in Figure B.5 will reveal more.

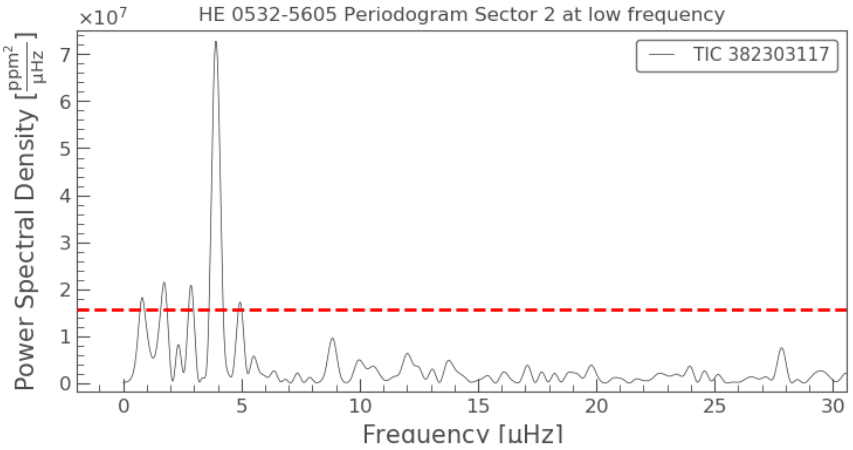

Figure B.5 This is the periodogram for Sector 2 at extremely low frequencies where an enormous peak can be found 3.93 μHz. Converting this into a period, the oscillations take roughly 2.95 days. This is due either to noise in the data set or possible relaxing effects from the possible outburst in Sector 1.

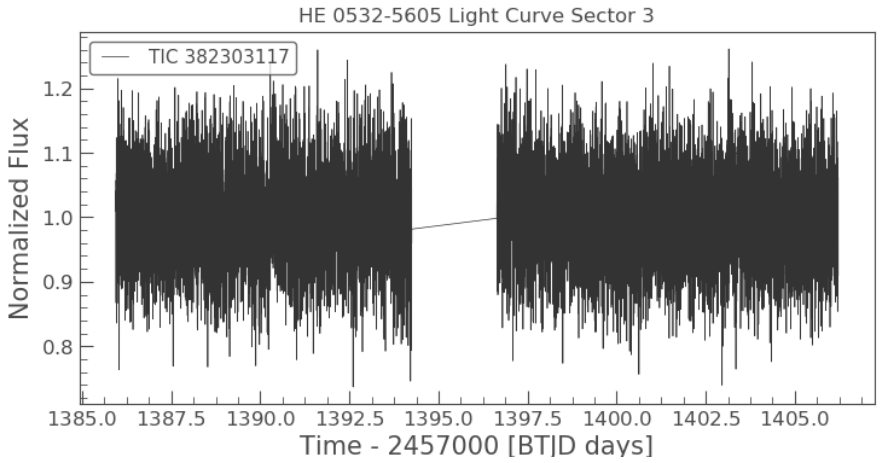

Figure B.6 This is the light curve produced in Sector 3. The mask used to make this light curve needed to be altered from the pipeline mask due to the pipeline misidentifying where the target was in frame. This was likely due to the very bright source nearby as seen in Figure 3.8.

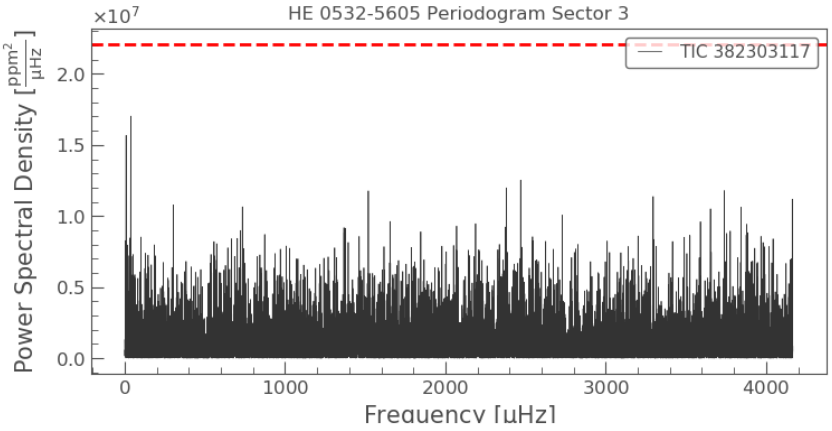

Figure B.7 This is the periodogram produced for Sector 3. Even with the corrected mask, it seems that the periodogram does not identify any frequencies that particularly rise above the background noise. This should be unusual for a DAV star.

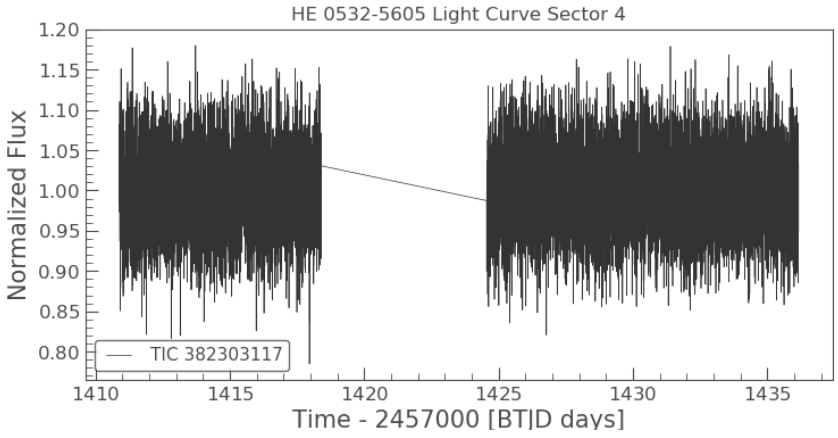

Figure B.8 This is the light curve produced for Sector 4, which had the lowest duty cycle of any of the sectors due to the Earth rising past the Sun-shade shortly after an instrument anomaly inhibited collection over 1.5 days of data.

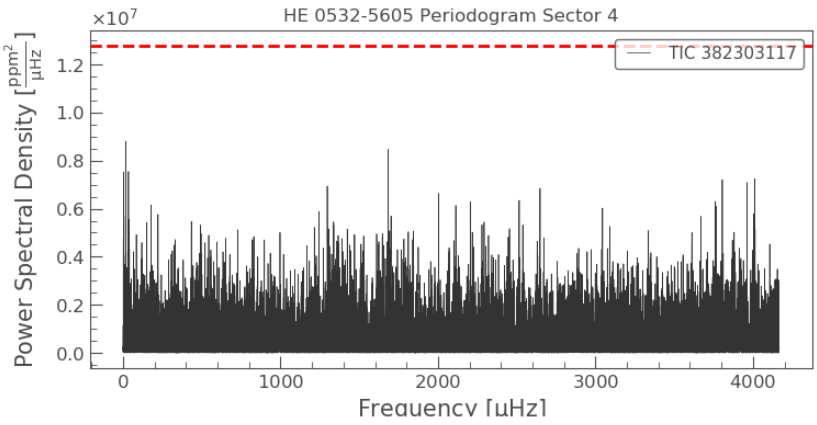

Figure B.9 This is the periodogram for Sector 4. No discernible frequencies were identified.

APPENDIX C. TABLE OF ACRONYMS

This is a table of the acronyms in alphabetical order used throughout this thesis for the reader's ease of reference.

Table C.1 A compiled list of acronyms used in this thesis

Acronym	**Expansion**
Amp	Amplitude (acquired via Lightkurve after correcting for Nyquist attenuation)
DAV	hydrogen-shell white dwarf pulsator
DRN	Data release notes
K2	Kepler: Second Light mission
LS Amp	Amplitude (acquired via least-squares fitting)
MAST	Mikulski Archive for Space Telescopes
mma	millimodulation amplitudes
PMT	Photo-multiplier tube
ppm	parts per million
PSD	Power spectral density
R548	Ross 548 (aka ZZ Ceti)
SNR	Signal-to-noise ratio
TASC	TESS Asteroseismic Science Consortium
Temp Corr	Amplitudes (acquired via Lightkurve and corrected for TESS bandpass and Nyquist attenuation)
TESS	Transiting Exoplanet Survey Satellite
TPF	Target pixel file
WET	the Whole Earth Telescope